Article

Molecular Cell

Dynamic Organization of Chromatin Domains Revealed by Super-Resolution Live-Cell Imaging

Graphical Abstract

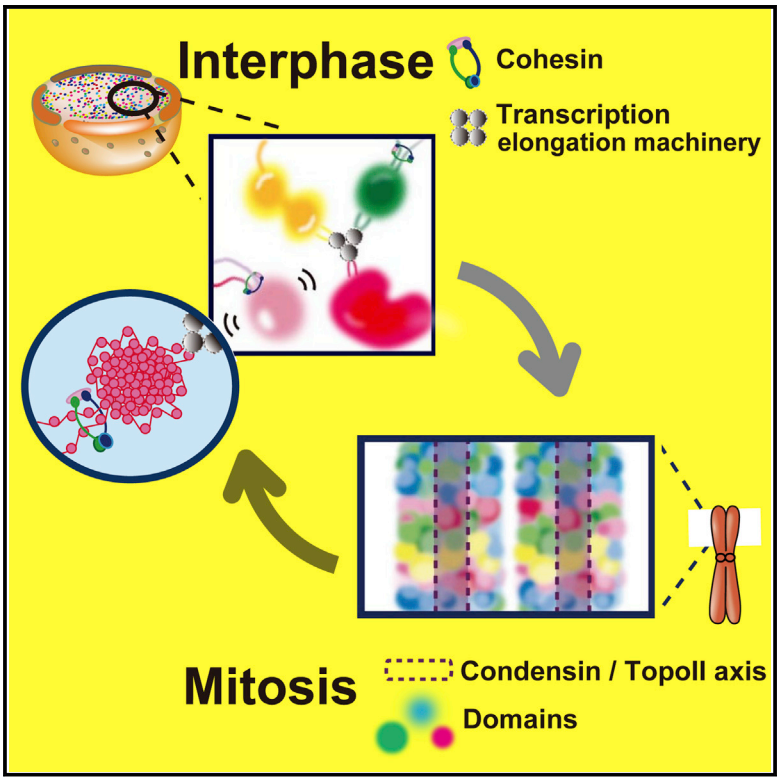

Authors

Tadasu Nozaki, Ryosuke Imai, Mai Tanbo, ..., Yasushi Okada, Takeharu Nagai, Kazuhiro Maeshima

Correspondence

kmaeshim@nig.ac.jp

In Brief

How a genome is organized and behaves in live cells remains unclear. Nozaki et al. visualized little bunches of chromatin, "chromatin domains," and their dynamic behavior in live mammalian cells. The domains can work as "Lego blocks" of chromosomes to maintain genetic information throughout the cell cycle.

Highlights

- We visualized chromatin structures and their dynamics in live mammalian cells
- Nucleosomes form compact chromatin domains in live cells and move coherently
- The domains are organized by nucleosome-nucleosome interactions and cohesin
- The domains exist during mitosis and act as building blocks of chromosomes

Nozaki et al., 2017, Molecular Cell 67, 282–293
July 20, 2017
http://dx.doi.org/10.1016/j.molcel.2017.06.018

CellPress

CellPress

Molecular Cell
Article

Dynamic Organization of Chromatin Domains Revealed by Super-Resolution Live-Cell Imaging

Tadasu Nozaki,[1,2] Ryosuke Imai,[1,3] Mai Tanbo,[1,3] Ryosuke Nagashima,[1,3] Sachiko Tamura,[1] Tomomi Tani,[4] Yasumasa Joti,[5] Masaru Tomita,[2] Kayo Hibino,[1,3] Masato T. Kanemaki,[6] Kerstin S. Wendt,[7] Yasushi Okada,[8] Takeharu Nagai,[9] and Kazuhiro Maeshima[1,3,10,*]

[1]Biological Macromolecules Laboratory, Structural Biology Center, National Institute of Genetics, Mishima, Shizuoka 411-8540, Japan
[2]Institute for Advanced Biosciences, Keio University, Fujisawa 252-8520, Japan
[3]Department of Genetics, School of Life Science, Sokendai (Graduate University for Advanced Studies), Mishima, Shizuoka 411-8540, Japan
[4]Eugene Bell Center for Regenerative Biology and Tissue Engineering, Marine Biological Laboratory, Woods Hole, MA 02543, USA
[5]XFEL Utilization Division, Japan Synchrotron Radiation Research Institute (JASRI), Sayo-gun, Hyogo 679-5198, Japan
[6]Division of Molecular Cell Engineering, National Institute of Genetics, Mishima, Shizuoka 411-8540, Japan
[7]Department of Cell Biology, Erasmus MC, 3000 CA Rotterdam, the Netherlands
[8]Laboratory for Cell Polarity Regulation, Quantitative Biology Center, RIKEN, Suita, Osaka 565-0874, Japan
[9]The Institute of Scientific and Industrial Research, Osaka University, Ibaraki, Osaka 567-0047, Japan
[10]Lead Contact
*Correspondence: kmaeshim@nig.ac.jp
http://dx.doi.org/10.1016/j.molcel.2017.06.018

SUMMARY

The eukaryotic genome is organized within cells as chromatin. For proper information output, higher-order chromatin structures can be regulated dynamically. How such structures form and behave in various cellular processes remains unclear. Here, by combining super-resolution imaging (photoactivated localization microscopy [PALM]) and single-nucleosome tracking, we developed a nuclear imaging system to visualize the higher-order structures along with their dynamics in live mammalian cells. We demonstrated that nucleosomes form compact domains with a peak diameter of ~160 nm and move coherently in live cells. The heterochromatin-rich regions showed more domains and less movement. With cell differentiation, the domains became more apparent, with reduced dynamics. Furthermore, various perturbation experiments indicated that they are organized by a combination of factors, including cohesin and nucleosome-nucleosome interactions. Notably, we observed the domains during mitosis, suggesting that they act as building blocks of chromosomes and may serve as information units throughout the cell cycle.

INTRODUCTION

Eukaryotic genomic DNA is organized three-dimensionally in cells as chromatin, which mediates various cellular functions for genomic information output (Bickmore, 2013; Cardoso et al., 2012; Hübner et al., 2013). Various recent studies have revealed that nucleosomes (10-nm fibers), consisting of DNA wrapped around the core histones (Luger et al., 1997), seem to be folded irregularly as local structures in vitro (Maeshima et al., 2016b) and in vivo (Chen et al., 2016; Eltsov et al., 2008; Fussner et al., 2012; Hsieh et al., 2015; Maeshima et al., 2016a; Ricci et al., 2015; Sanborn et al., 2015).

For higher-order chromatin structures, a number of structural models have been investigated: "chromonema fibers" with a diameter of 100–200 nm based on hierarchical helical folding (Kireeva et al., 2004) and DNA replication foci domains with an average diameter of approximately 110–150 nm observed via pulse labeling (Albiez et al., 2006; Baddeley et al., 2010; Cseresnyes et al., 2009; Jackson and Pombo, 1998; Markaki et al., 2010). Recently, chromosome conformation capture (3C) and related methods (Dekker and Heard, 2015) have revealed contact probability maps of genomic DNA in formaldehyde (FA)-fixed cells. These maps suggest that numerous chromatin domains are formed as functional units of the genome, designated "topologically associating domains" (TADs) (Dixon et al., 2012; Nora et al., 2012; Sexton et al., 2012) or "contact domain/loop domain" (Rao et al., 2014; Sanborn et al., 2015).

However, how such higher-order structures are formed and then behave in various cellular processes in live cells remains unclear. To obtain an integrated view of higher-order structures and their dynamics in live mammalian cells, we utilized a combination of photoactivated localization microscopy (PALM) (Betzig et al., 2006; Boettiger et al., 2016; Manley et al., 2008; Rust et al., 2006; Ricci et al., 2015) and single-nucleosome tracking (Hihara et al., 2012; Nozaki et al., 2013). We demonstrated that nucleosomes form compact domains in live cells during mitosis as well as interphase. The organization and dynamics of the domains are affected by various factors, including cohesin (Nasmyth and Haering, 2005; Shintomi and Hirano, 2010; Uhlmann, 2016) and nucleosome-nucleosome interactions (Funke et al., 2016; Kalashnikova et al., 2013). We suggest that our observed chromatin domains are the building blocks of chromosomes throughout the cell cycle.

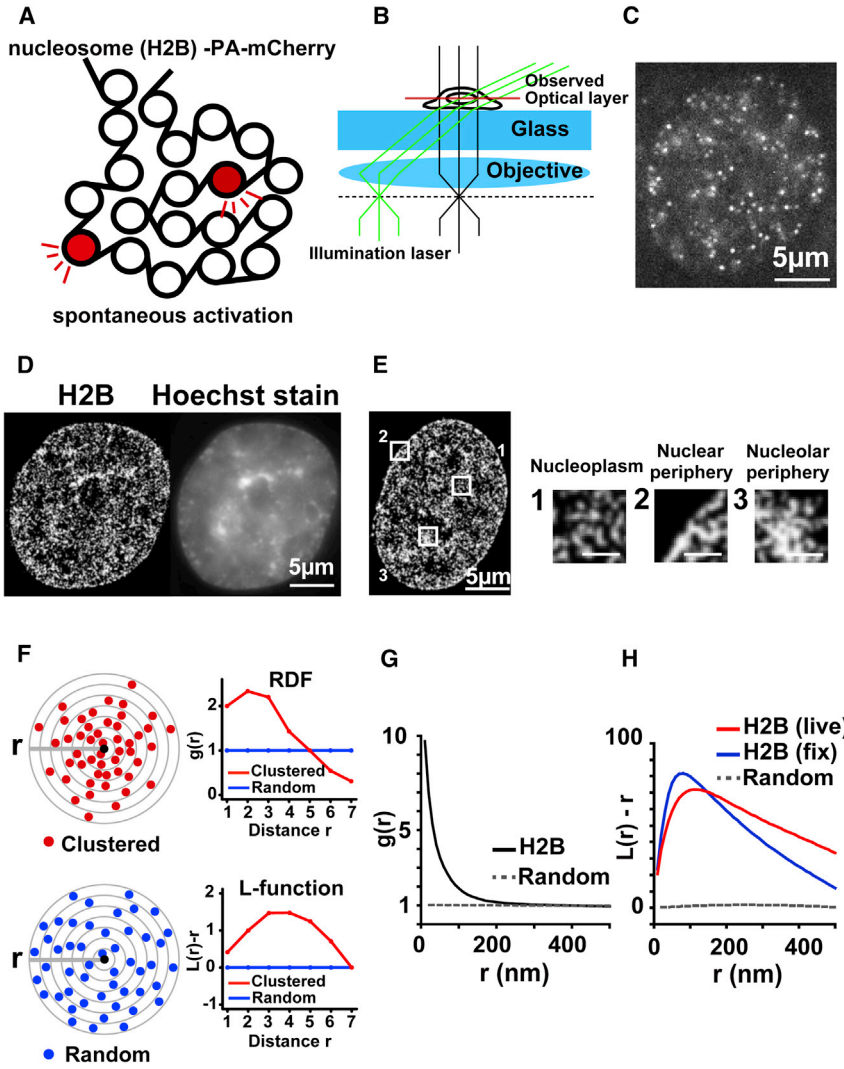

Figure 1. PALM Imaging and Chromatin Domain Analysis

(A) Histone H2B-PA-mCherry activation for live PALM imaging and single-nucleosome tracking.

(B) Scheme of oblique illumination microscopy. Using a sheet light (green), only a thin optical layer within the nucleus (red) was illuminated.

(C) Single-nucleosome (H2B-PA-mCherry) image of the nucleus of a live HeLa cell.

(D) Live-cell PALM image of histone H2B (left) and correlative Hoechst 33342 DNA staining of the same live cell (right). Shown is a representative image of ten PALM images.

(E) Live-cell PALM image of histone H2B (left) and magnified images (right) from the boxed regions in the image. Shown is a representative image of 20 PALM images. Scale bars, 1 μm.

(F) A simplified scheme for radial distribution function (RDF) (upper) and L-function (lower) analyses. Shown are clustered (red spheres, top left) or random (blue spheres, bottom left) particles around the origin point (black sphere). RDF (top) and L-function (bottom) plots of a random pattern (blue) are ~1 and 0, respectively. For more details, see Figure S1F.

(G) RDF plots of interphase chromatin (black) and random distribution plots (gray dotted line) (n = 75 cells).

(H) The L-function plot of interphase chromatin (red) in live cells shows a curve with a peak at ~110 nm (i.e., ~220 nm in diameter), and formaldehyde (FA)-fixed interphase chromatin (blue) shows a peak at ~80 nm (i.e., ~160 nm in diameter), whereas the plot of the random distribution model with the same density dots (Figure S1G) as the PALM image is almost zero (n = 75 live cells and n = 10 FA-fixed cells).

See also Figure S1.

RESULTS

Chromatin Domain Structures in Live Cells

To combine PALM (Betzig et al., 2006; Rust et al., 2006) and single-nucleosome tracking (Hihara et al., 2012; Nozaki et al., 2013), we fused histone H2B with photoactivatable (PA)-mCherry (Subach et al., 2009), which acquires fluorescence upon UV laser stimulation, and expressed the fusion protein in HeLa cells (Figure 1A; Figure S1A). The modified histone H2B is incorporated into the nucleosomes throughout the genome by histone replacement on a scale of hours (Kimura and Cook, 2001). We used oblique illumination microscopy for imaging of chromatin, which allowed us to illuminate a thin area within a single nucleus (green lines in Figure 1B; Tokunaga et al., 2008). Using this system, we found that a relatively small number (~100/time frame (50 ms)/nucleus) of H2B-PA-mCherry molecules were continuously and stochastically activated even without UV laser stimulation (Figure 1A). Clear, well-separated dots were detected (Figure 1C), with a single-step photobleaching profile (Figures S1B and S1C), which suggested that each dot represents a single H2B-PA-mCherry molecule in a single nucleosome. Every time frame, ~100 dots appeared upon activation and diminished ~0.05–1 s (~1–20 frames) later by photobleaching (Movie S1). In addition, stepwise salt washing of nuclei isolated from the H2B-PA-mCherry-expressing cells confirmed that ectopically expressed H2B-PA-mCherry behaved similar to endogenous H2B (Figure S1D), suggesting that the H2B-PA-mCherry molecules were incorporated properly into the nucleosomes in these cells.

We recorded the PA-mCherry-nucleosome dots in the interphase chromatin at 50 ms/frame (~1,000 frames, 50 s total) in live cells (Movie S1). The PA-mCherry dots were fitted with a 2D Gaussian function to estimate the precise position of the nucleosome (the position determination accuracy is 20.02 nm; see STAR Methods). Note that only the PA-mCherry nucleosomes in a thin layer of ~200-nm thickness are detected, as shown by the point spread function (PSF) of the PA-mCherry signal measured in the cells (Figure S1E), excluding the projection effect from different focal distances.

We first examined the spatial organization of nucleosomes from the live-cell PALM images obtained this way, each of which consisted of ~80,000 nucleosome dots/optically sectioned focal plane (~200-nm thickness) of the nucleus. Among the dots, ~20,000 are expected to be unique. Considering the thickness of the optical section, the measured nuclear thickness (~7 μm), and the expected total numbers of nucleosomes in HeLa cells (~4.5 × 10^7 nucleosomes/HeLa nucleus), approximately 2% of the total nucleosomes in the section volume were labeled and examined. These nucleosome dots appeared to be highly clustered in live cells (Figures 1D and 1E). Higher levels of clustering seemed to be located around the nuclear periphery and edges of nucleoli (Figure 1E) or in regions with stronger Hoechst (DNA) signals (Figure 1D).

To verify whether the nucleosomes were actually clustered versus distributed randomly, we utilized a radial distribution function (RDF) (Bohn et al., 2010). RDF or g(r) refers to the density of the nucleosomes in the circular ring, at a distance between r and r + Δr from the reference point, and thus gives a value of ~1 for the random distribution [(g)r ~1] (Figure 1F; Figure S1F). The measured RDF shown in Figure 1G showed a marked increase of g(r) in the range of 0 to ~250 nm, quantitatively supporting the clustering or domain formation of nucleosomes in live cells.

In the following analyses, we mainly used the L-function, L(r) (Figure 1F; Figure S1F), because the plot of L-function (L(r)-r versus r plot) gives a value of 0 for the random distribution, and deviation from zero provides an intuitive measure of the size of the cluster and the degree of accumulation (Figures 1F and 1H; Figures S1F and S1G). Computational modeling for chromatin condensation and decondensation states (Figure S7) suggests that the L-function plot peak can provide good approximations of the size and compaction state of the domains.

The L-function plot shown in Figure 1H shows a single peak at ~110 nm for normal live cells, suggesting that the typical size of the domains is approximately 220 nm in diameter. In FA-fixed cells, the L-function plot sharpened, corresponding to a domain size of approximately 160 nm in diameter (Figure 1H). These results suggest that chromatin domain structures are observed in both live and chemically fixed cells. Note that the measured domain size in live cells became larger than that in FA-fixed cells (Figure 1H), presumably because of the "motion blur effect" that increased chromatin movement results in blurred structural features.

Chromatin Domain Dynamics in Live Cells

Because our movie data (20 frames/s; Movie S1) also contained information on nucleosome movements in a thin optical layer, we next examined the dynamics of the chromatin domains in live cells based on movements of individual nucleosomes (Figure 2A). We first tracked each nucleosome movement from 0 to ~0.5 s (~11 frames) using u-track software (Figure 2B; Jaqaman et al., 2008). About 60 nm of nucleosome movement for 50 ms was observed (Figure S2A), consistent with our previous studies (Hihara et al., 2012). The plots of calculated mean square displacement (MSD) were well fitted to an anomalous diffusion model (Control in Figure 2C). Chemical fixation of the cells with disuccinimidyl glutarate (DSG) and FA to crosslink nucleosomes severely suppressed the movements (Figure 2C), indicating that most of the observed movement was derived from real nucleosome movements in live cells.

We then examined whether the observed movement of the individual nucleosomes reflects the dynamics of the domains to which they belong. To address this question, we utilized DNA replication foci domains with an average diameter of approximately 110–150 nm (Baddeley et al., 2010; Cseresnyes et al., 2009; Markaki et al., 2010) composed of certain genomic DNA regions labeled by incorporation of cyanine 3-deoxycytidine triphosphate (Cy3-dCTP) during DNA replication (Figure 2D). Consistent with previous publications (e.g., O'Keefe et al., 1992), we observed, in labeled asynchronous cells, early and mid-late replication foci patterns (Figure S2B). Because we could not define the boundaries of the replication domains, to investigate the dynamics of these foci, we tracked the centers of foci in 30 randomly selected live cells and calculated the MSD, which revealed that the dynamics of early replication domains were higher than those of mid-late domains (Figure S2C).

We then compared the movements of the nucleosomes and DNA replication domains (Figure 2E). Interestingly, the MSD plot of nucleosome movement was similar to that of domain movement (early and mid-late) (Figure 2F). To further pursue the results from MSD, dual-color labeling and imaging of the nucleosomes (H2B-Halo with green dye, R110) and replication domains (red dye, Cy3) were performed (Figure 2E). Although it was very rare to find situations in which a single H2B-R110 and a single Cy3-dCTP focus are close together, such 26 trajectory sets revealed their correlated movements (Figure 2G; left, Figure 2H), suggesting that the nucleosomes and their putative domains moved similarly (Figures 2G and 2H; Movies S2 and S3). On the other hand, the nucleosomes and domains far away from them (a total of 28 trajectory sets) moved independently (right, Figure 2H). Considering that the observed movement of the replication domain represents centroid movement of the fluorescent molecules distributed over the domain (>10–20 dyes/domain; right, Figure 2E; STAR Methods), our findings showed that, at least, most of the nucleosomes form domains in live cells and that they move coherently (Figure 2I). Therefore, as an approximation, we used nucleosome movement to represent domain dynamics in subsequent analyses.

Heterochromatin-Rich Regions Show Less Movement

In addition to MSD analysis, which calculates the ensemble average of domain movement, we integrated the movement data on a 2D plane to visualize the magnitude of chromatin domain dynamics as a 2D heatmap ("chromatin heatmap") (Figures 2J and 2K). Here, larger domain movement appears as more "red" (or hot), and smaller movement appears as more "blue" (or cold) pixels (Figure 2J). This heatmap provides spatial domain dynamics in the whole nucleus of a live cell (Figure 2K). On the heatmap (Figure 2K), the nuclear periphery (box 2) and edges of nucleoli (box 3), which were presumably heterochromatin-rich regions (Lemaître and Bickmore, 2015), showed less movement.

Consistently, when we focused on nuclear bottom surfaces (Shinkai et al., 2016), the L-function plot was higher than that in

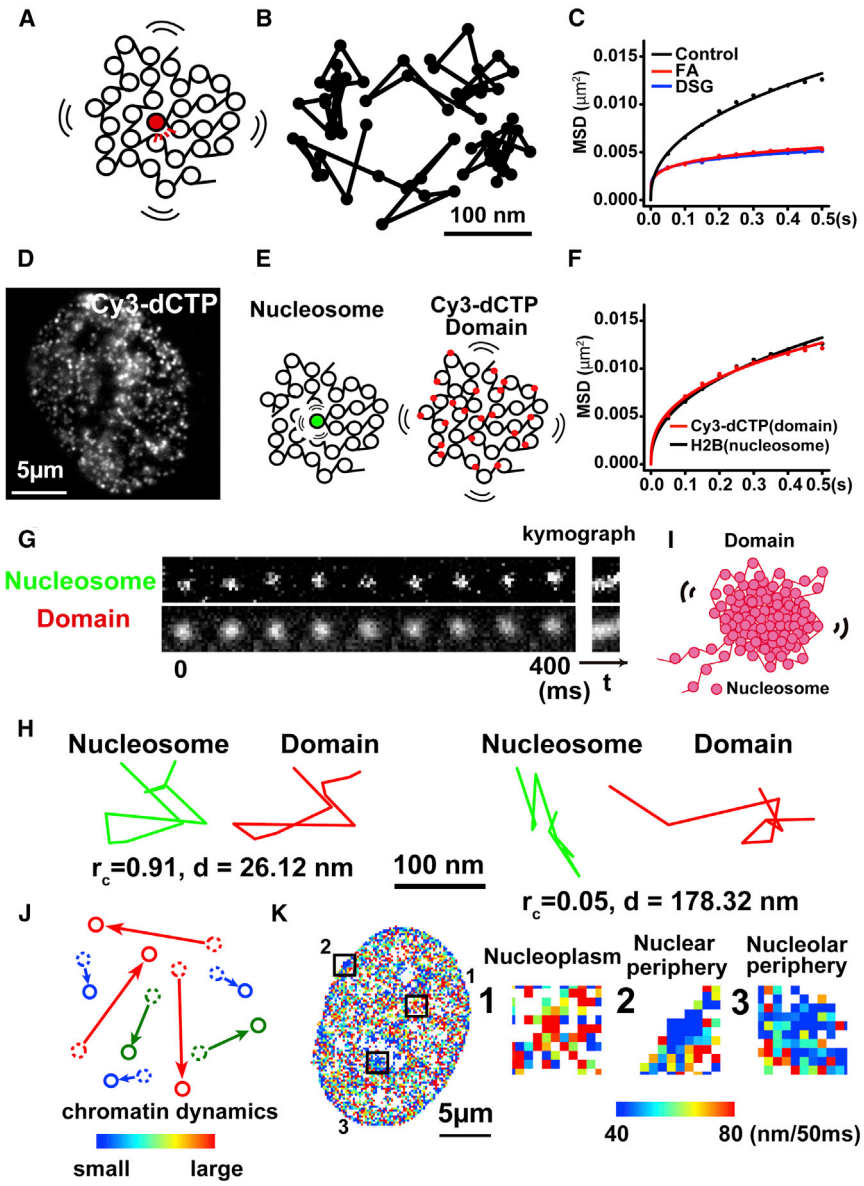

Figure 2. Visualization of Chromatin Domain Dynamics

(A) Scheme for visualization of chromatin domain dynamics based on single-nucleosome tracking.

(B) Representative tracked trajectories of single nucleosomes.

(C) Mean square displacement (MSD) plots of single nucleosomes in interphase chromatin of live (black), FA-fixed (red), and disuccinimidyl glutarate (DSG)-fixed HeLa cells (blue) from 0–0.5 s. For each sample, n = 15–75 cells.

(D) Image of DNA replication foci labeled by Cy3-dCTP in the nucleus of a live HeLa cell.

(E) Scheme for dual-color labeling and imaging of the nucleosomes (left) with H2B-Halo-R110-incorporated (green dye) and Cy3 (red dye)-incorporated DNA replication domains (right).

(F) MSD plots of DNA replication domains (red, n = 30 cells) compared with those of nucleosomes (black, n = 75 cells) from 0–0.5 s.

(G) A representative example showing correlative movements of nucleosomes and their putative domains (see also Movies S2 and S3).

(H) Representative trajectories of correlative (left) and non-correlative (right) movements between the nucleosomes (green) and domains (red).

(I) A model showing that nucleosomes form a domain and move coherently (see also Figures 7A and 7C).

(J) Scheme of chromatin heatmaps. In the heatmap, small movements are shown in blue, and large movements are shown in red.

(K) The chromatin heatmap for 50 ms in a live HeLa cell (left) and magnified images (right) from the boxed regions in the heatmap.

See also Figure S2.

nuclear interiors, suggesting a clustering of domains at the nuclear periphery (Figure S2D). On nuclear surfaces, the domain dynamics slowed down (Figure S2E), and the chromatin heatmap turned more blue (Figure S2F), probably because of the tethering of the domains to inner nuclear membrane structures (Lemaître and Bickmore, 2015). In good agreement, the dynamics of mid-late replication domains, which are heterochromatin-rich regions around the nuclear periphery (Ryba et al., 2010), were lower than those of the early domains (Figure S2C).

Chromatin Domains Are Organized by Nucleosome-Nucleosome Interactions and Cohesin Complexes

We performed a series of perturbation experiments to determine the types of biochemical and physicochemical factors involved in domain formation and dynamics. We first examined the role of nucleosome-nucleosome interactions by treatment with the histone deacetylase (HDAC) inhibitor trichostatin A (TSA). Inhibition of HDAC by TSA increases histone tail acetylation, including lysine 16 of histone H4 (Figure S3A). Histone tail acetylation by TSA treatment led to global decondensation of chromatin texture (Görisch et al., 2005; Ricci et al., 2015), presumably by weakening the H3 and H4 tail binding to the neighboring nucleosome and subsequent inhibition of nucleosome-nucleosome interactions (Kalashnikova et al., 2013). Consistent with this notion, TSA-treated cells exhibited more distributed nucleosome signals throughout the nucleus than control cells (Figure 3A), whereas the nuclear volumes did not change (Figure S3B). The peak position and height of the L-function plot by TSA treatment decreased (Figure 3B), which showed that increased histone acetylation by TSA treatment decondensed the chromatin domains (Figure 3B). Histone acetylation also led to increased dynamics (Figures 3C and 3D; Figure S4A), presumably because decondensation of the chromatin domains made the chromatin more flexible and mobile. Importantly, after TSA treatment, FA-fixed cells still showed a decrease in the

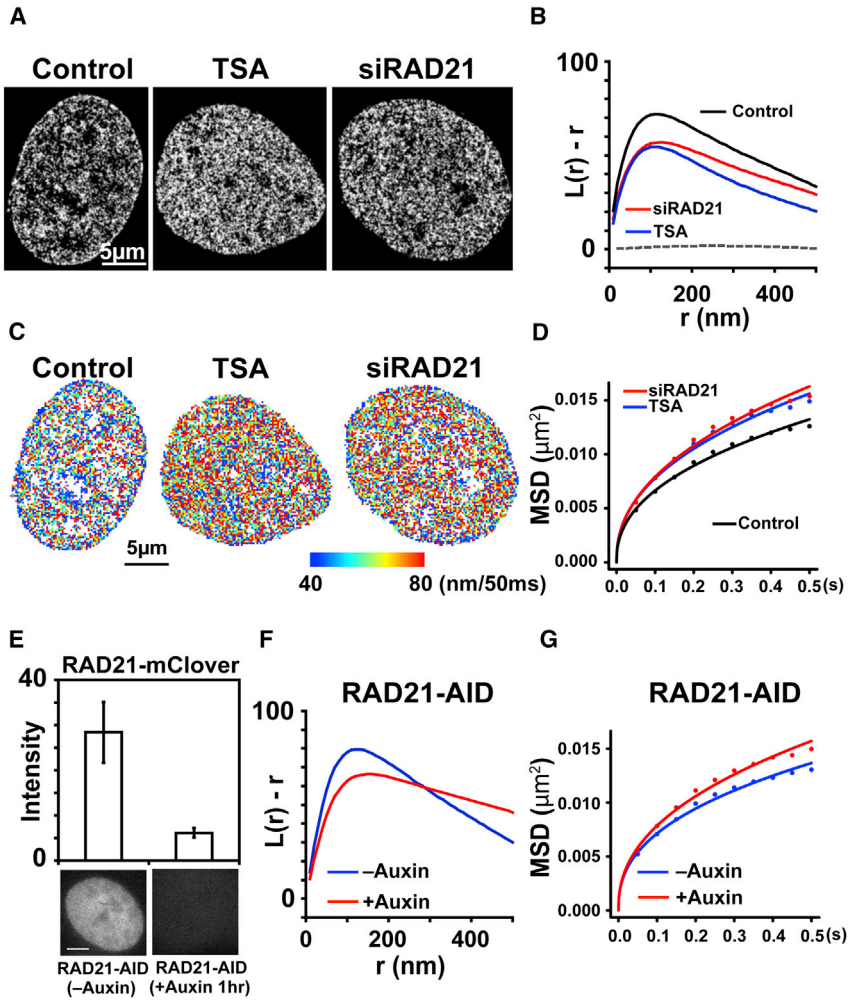

Figure 3. Involvement of Nucleosome-Nucleosome Interactions and Cohesin in Domain Formation and Dynamics

(A) PALM images of interphase chromatin based on H2B-PA-mCherry in live HeLa cells. From left to right, shown are a control (untreated) cell, a trichostatin A (TSA)-treated cell, and a RAD21 knockdown (KD) cell.

(B) L-function plots of chromatin with the same conditions as in (A). For each condition, n = 25–75 cells.

(C) Chromatin heatmaps for 50 ms in a live HeLa cell (control), TSA-treated cell, and RAD21-KD cell.

(D) MSD plots of the domains in HeLa RAD21-KD cells (red), TSA-treated cells (blue), and control cells (black) from 0–0.5 s. For each condition, n = 25–75 cells. For plots with SD, see Figure S4A.

(E) Fluorescent image of RAD21-mClover in live HCT116 cells (left) and cells treated with auxin for 1 hr (right).

(F and G) L-function plots (F) and MSD (G) for RAD21-mAID-Clover HCT116 cells treated with auxin (red) and without auxin (blue). For each condition, n = 12–15 cells.

See also Figure S3.

L-function plot (Figures S3C and S3D), excluding the possibility that the observed decondensation effect of the treatment was due to increased movement of the domains (i.e., the motion blur effect). These results suggest that nucleosome-nucleosome interactions contribute to the formation of chromatin domains and restrict their dynamics (Figures 2I, 7A, and 7B), whereas histone acetylation may lead to the recruitment of other chromatin remodeling complexes and transcription factors, as well as further decondensation. Our findings also suggest that chromatin domain organization and dynamics can be controlled by histone modifications.

We next investigated whether the cohesin complex is involved in chromatin domain formation and dynamics. Cohesin can capture chromatin fibers within its ring structure, thereby forming loops and subsequent higher-order chromatin structures (Nasmyth and Haering, 2005; Shintomi and Hirano, 2010; Uhlmann, 2016). When the cohesin subunit RAD21 was depleted (Figure S3E) by small interfering RNA (siRNA) (Wendt et al., 2008), the nucleosomes were distributed more uniformly in the nucleus, with higher mobility, causing decondensation of the domains (Figures 3A–3D; Figure S4A). The peak position and height of the L-function plot decreased to similar levels as those seen with TSA treatment (Figure 3B). In addition, knockdown (KD) of the cohesin loader NIPBL (Figure S3F; Zuin et al., 2014b) had similar effects as KD of RAD21 (Figures 4A and 4B; Figure S5C).

Interestingly, treatment with both TSA and RAD21-KD resulted in more marked effects (Figures S4B and S4C), suggesting their cooperation. Conversely, neither treatment was effective on chromatin domains around the nuclear surface/periphery (Figure S4D), which is probably due to tethering of the domains to the inner nuclear membrane structures (Lemaître and Bickmore, 2015).

To exclude the possibility that prolonged treatment with RAD21 or NIPBL siRNA (60 or 72 h) had various indirect effects on chromatin structure, we performed imaging of human HCT116 cells rapidly depleted of RAD21 protein using auxin-inducible degron (AID) technology (Natsume et al., 2016). One hour after auxin addition, RAD21 had disappeared (Figure 3E), and, consistent with the siRNA results, the domains had decondensed and their dynamics increased (Figures 3F and 3G). This strongly supports the critical function of cohesin in chromatin domain organization and dynamics (for a model, see Figures 7A and 7B).

We then examined other protein factors that could affect chromatin structure and dynamics. KD of CCCTC-binding factor (CTCF) (Figure S5A; Wendt et al., 2008), which is also involved in loop formation, together with cohesin, did not change the L-function or MSD plots (Figures 4A and 4B; Figure S5C). Simultaneous KD of both CAP-H2 and G2 in the condensin II complex (Figure S5B), which is localized within interphase nuclei and functions in sister chromatid resolution during S phase (Ono et al., 2013), only caused slight

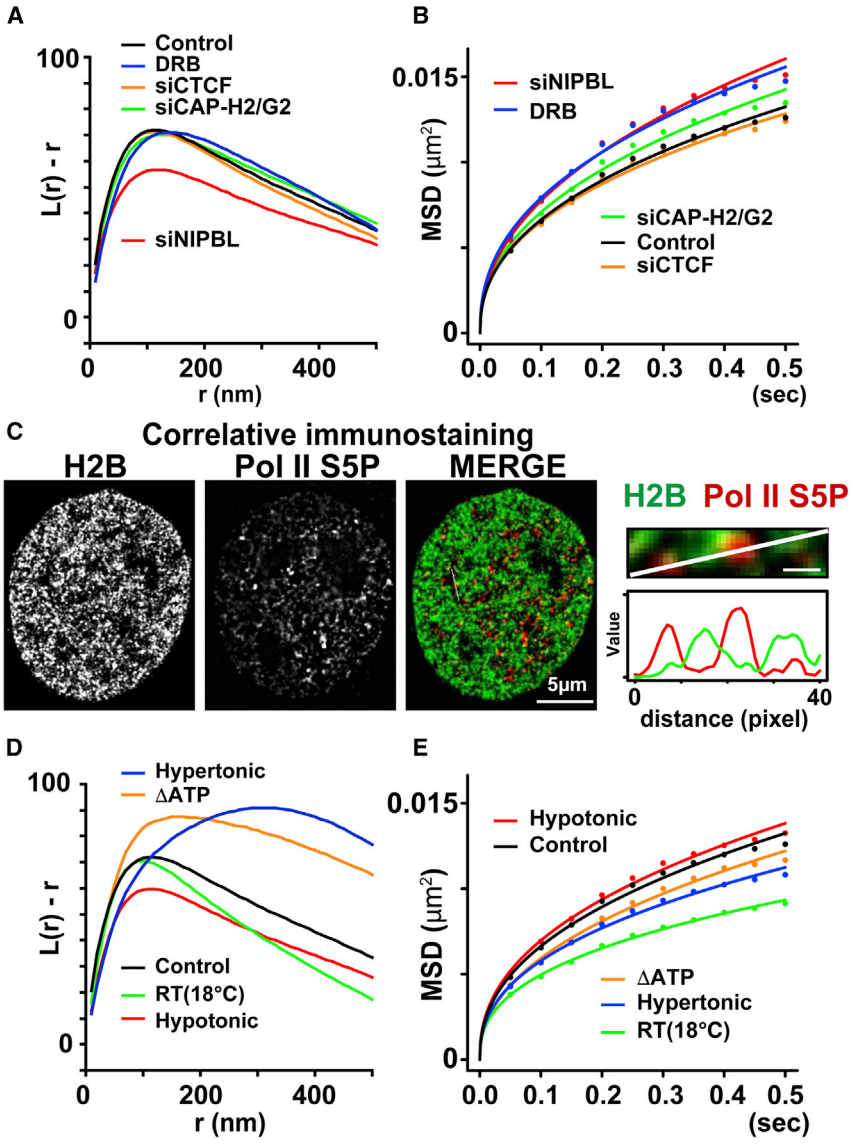

Figure 4. Various Perturbation Experiments on Domain Formation and Dynamics

(A and B) L-function (A) and MSD (B) plots of chromatin in NIPBL-KD cells (red), CAP-H2/G2-KD cells (green), CTCF-KD cells (orange), 5,6-Dichloro-1-β-D-ribofuranosylbenzimidazole (DRB)-treated cells (blue), and control cells (black). For each condition, n = 25–75 cells.

(C) Left: correlative immunostaining with anti-RNA Pol II phospho-Ser5 antibody to mark active RNA Pol II on the same H2B-PA-mCherry-expressing cell after PALM imaging. Shown is a representative image of eight cells. Another example is provided in Figure S5D. Also shown are overlay images of PALM (green) and Pol II phospho-Ser5 staining (red). Right: magnified image from the white line region in the left merge image. Scale bar, 500 nm. The mutually exclusive pattern of chromatin (green) and active Pol II (red) on the white line is also indicated by an intensity line scan.

(D and E) L-function (D) and MSD (E) plots of chromatin in hypertonic cells (blue), hypotonic cells (red), ATP-depleted cells (orange), cells observed at room temperature (RT, 18°C) (green), and control cells (black). For each condition, n = 20–75 cells.

See also Figure S5.

changes in L-function and MSD plots (Figures 4A and 4B; Figure S5C).

Transcription Inhibition Does Not Affect Domain Structure but Increases the Dynamics

Furthermore, to examine the role of the transcriptional process in domain structure and dynamics, we treated cells with 5,6-Dichloro-1-β-D-ribofuranosylbenzimidazole (DRB), which is a selective inhibitor of transcription elongation by RNA polymerase II (RNA Pol II) in eukaryotic cells (Kwak and Lis, 2013) and dissociates the RNA Pol II elongation complex (Kimura et al., 2002). Although this treatment markedly suppressed global RNA synthesis in the cells (Figure S5E), it did not alter domain formation (Figure 4A; Figure S5C). However, DRB treatment increased the domain dynamics (Figure 4B), suggesting that, although RNA Pol II activity is not directly involved in domain maintenance, some domains are stabilized during transcriptional elongation (for a model, see Figure 7A). Dissociation of the elongation complexes by DRB treatment (Kimura et al., 2002) may release the constraints on the domains and increase the domain dynamics.

Consistent with this finding, correlative immunostaining of the same cells after live-cell PALM imaging with an active RNA Pol II marker, anti-phosphorylated serine 5 antibody (Stasevich et al., 2014), revealed that the active RNA Pol II clusters were often localized outside of the chromatin domains (Figures 4C and 7A; Figure S5D), in accordance with some previous reports (Markaki et al., 2010).

Physicochemical Factors Are Also Involved in Chromatin Domain Formation and Dynamics

Next we turned our attention to physicochemical factors of chromatin domain formation and dynamics. We first changed the osmotic pressure, which could be related to intracellular cations and macromolecular crowding conditions (Albiez et al., 2006). Hypo-osmotic conditions with dilute medium (~140 mOsm instead of the normal ~290 mOsm) led to decondensation of domains (Figure 4D; Figure S5C), although this treatment did not alter the domain dynamics (Figure 4E), suggesting that the molecular crowding force and cations contribute to the domain structure but not dynamics (see Discussion). On the other hand, hypertonic treatment (~570 mOsm) had the opposite effect and caused chromatin

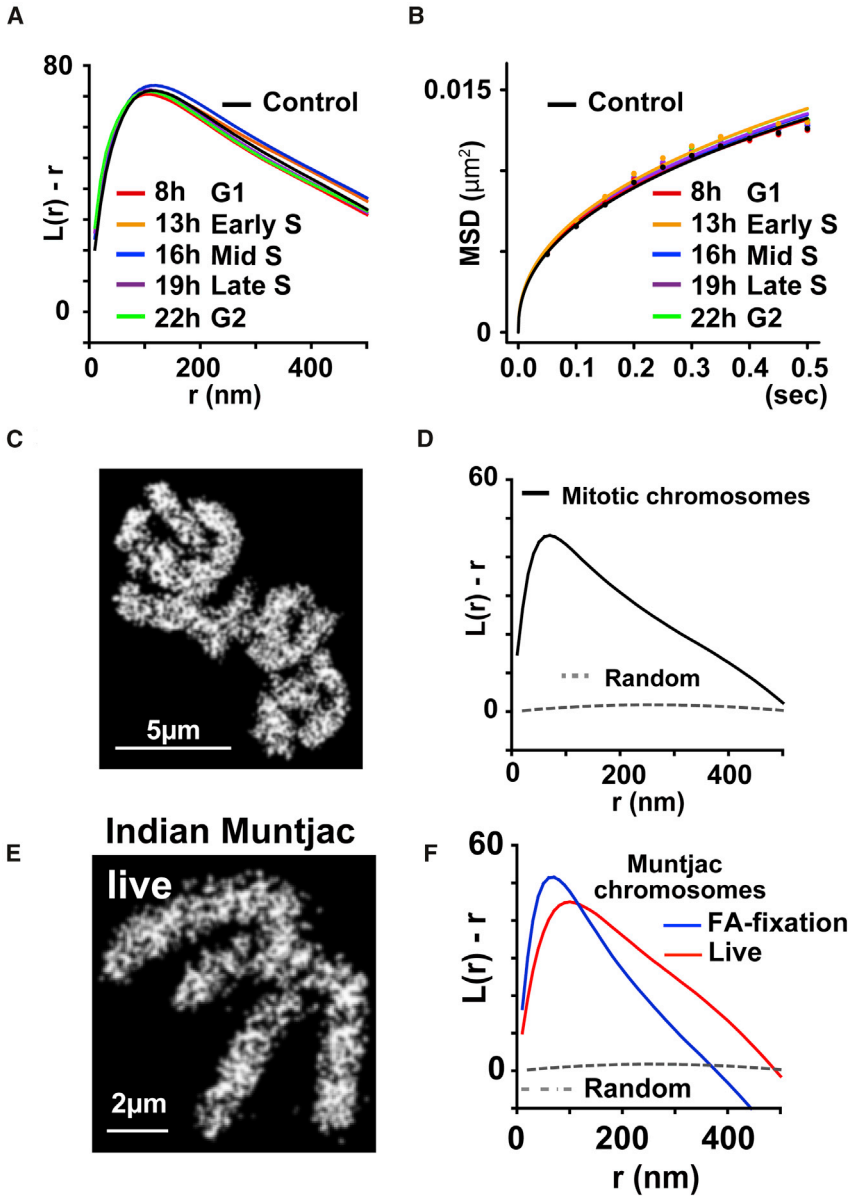

Figure 5. Domain Structure in Mitotic Chromosomes

(A and B) L-function (A) and MSD (B) plots of chromatin during various stages of the cell cycle. Times after mitotic release are shown; asynchronous control, black. For flow cytometry data, see Figure S6A. For each condition, n = 25–75 cells.

(C) PALM image of mitotic chromosomes based on H2B-PA-mCherry in FA-fixed HeLa cells.

(D) L-function plots of chromatin in FA-fixed HeLa mitotic chromosomes (n = 20 cells).

(E) PALM images of mitotic chromosomes based on H2B-PA-mCherry in live Indian muntjac DM cells.

(F) L-function plots for mitotic live and FA-fixed DM cells demonstrate that the nucleosomes formed compact chromatin domains during muntjac cell mitosis. For live and fixed cells, n = 11 and 16 cells, respectively.

See also Figure S6.

Similar Domain Structures Are Observed in Mitotic Chromosomes

We investigated the behavior of the chromatin domains during the cell cycle. A time course experiment for PALM imaging was performed using synchronized HeLa cells that were released from mitotic arrest and verified by flow cytometry (Figure S6A). We observed similar chromatin domains and dynamics from G1, S, and G2 phases, suggesting that the chromatin structure does not change significantly throughout interphase (Figures 5A and 5B).

We next focused on mitosis. Chromosome fluctuation, which reflects chromosome congression (Iemura and Tanaka, 2015), is prominent in live mitotic HeLa cells; therefore, we first examined fixed cells and found chromatin domain structures in mitotic chromosomes. The PALM images demonstrated highly clustered nucleosomes in the FA-fixed mitotic chromosomes (Figure 5C), which were also revealed by RDF analysis (Figure S6B). L-function plots demonstrated that the fixed mitotic chromosomes had a notable peak with a diameter of ~140 nm (Figure 5D), which is comparable with that of interphase domains (Figure 1H).

We then studied mitotic chromosomes using Indian muntjac DM cells (Hihara et al., 2012; Manders et al., 1999), which have large chromosomes and are less mobile and advantageous for this type of analysis. The mitotic chromosomes in fixed and live muntjac cells had peak diameters of ~140 nm and ~200 nm, respectively (Figures 5E and 5F; Figure S6C). A heatmap of muntjac chromosomes showed "non-uniform" movements of nucleosomes (Figure S6D). Taken together, these results suggest the existence of chromatin domain structures in mitotic chromosomes in live cells. Notably, the values obtained in mitotic chromosomes are in good agreement with those

hypercondensation (Figure 4D; Figure S5C) along with reduced dynamics (Figure 4E).

ATP depletion of cells treated with sodium azide and 2-deoxyglucose (Figure S5F) condensed the chromatin domains and slightly decreased the dynamics (Figure 4D and 4E; Figure S5C) (see Discussion). Reduction of the temperature of the cells from 37°C to 18°C caused a marked chromatin domain slow-down (Figure 4E), although the domain organization did not change significantly (Figure 4D; Figure S5C). Importantly, these findings regarding the physicochemical factors suggest that the structural and dynamic aspects of the domains can be well separated, even in live cells, and may also be critical physical parameters for computational modeling of chromatin and chromosomes (Cheng et al., 2015; Ozer et al., 2015; Shinkai et al., 2016).

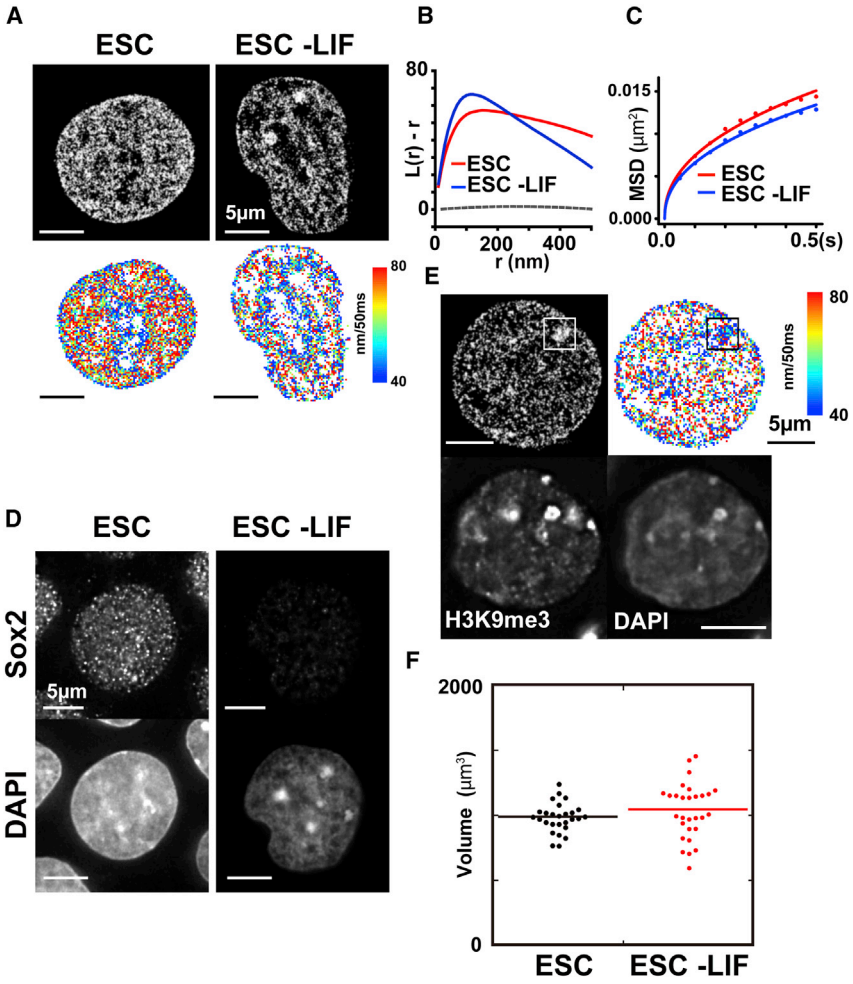

Figure 6. Chromatin Domain Structure and Dynamics in Mouse ESCs

(A) PALM images and chromatin domain heatmaps for embryonic stem cells (ESCs) and ESC-LIF ESCs that were cultured in medium without the differentiation inhibitory factor (leukemia inhibitory factor [LIF]) for 5 days.

(B and C) L-function (B) and MSD (C) plots of chromatin in ESCs (red) and ESC-LIF (blue). n = 35–40 cells.

(D) Immunostaining of ESCs and ESC-LIF cells incubated with anti-Sox2 antibody and DAPI.

(E) Live-cell PALM image (top left) and chromatin heatmap (top right) in the chromocenter (box) of an ESC, showing chromatin condensation and decreased domain dynamics in the region. The chromocenter region was confirmed by correlative immunostaining with anti-H3K9me3 antibody (bottom left) and DAPI staining (bottom right) after PALM imaging. Scale bar, 5 μm.

(F) Effect of differentiation on nuclear volume.

in interphase cells (Figure 1H). Our findings also suggest that the chromatin domains may be retained throughout the cell cycle (for a model, see Figure 7A).

Chromatin Domains Become More Apparent with Cell Differentiation

To study the behavior of chromatin domains during cell differentiation, we established mouse embryonic stem cells (ESCs) expressing H2B-PA-mCherry and performed live-cell PALM imaging (Figure 6A). Interestingly, the L-function plot in ESCs was a rather flat curve (Figure 6B), suggesting that ESCs have more decondensed chromatin than HeLa cells, that the domain structure may not be well-defined, and that the dynamics are greater (Figures 6A and 6C), consistent with previous reports (Meshorer and Misteli, 2006; Ricci et al., 2015). Chromatin heatmap analysis revealed higher domain dynamics in ESCs than in HeLa cells (Figures 2K and 6A). On the other hand, the nuclear periphery and the chromocenters (pericentromeric heterochromatin), which were confirmed by correlative immunostaining of the heterochromatin marker trimethylation of histone H3 Lys9 (H3K9me3), showed reduced domain dynamics (box in Figure 6E), consistent with the results obtained from nuclear surfaces (Figures S2E and S2F).

Because the rather ambiguous chromatin domains and "hot" chromatin properties of the ESCs may be related to their pluripotency, we induced embryoid body (EB) formation by depletion of leukemia inhibitory factor (LIF) from ESCs. The pluripotent marker Sox2 was not detectable in the cells, ensuring differentiation toward EBs (ESC-LIF in Figure 6D). After differentiation, the nuclear volumes did not change (Figure 6F), but the L-function plots showed a sharper peak (ESC-LIF in Figure 6B), indicating that the chromatin domains had become more defined. MSD analysis also showed that the domain dynamics decreased, with more blue color observed in the heatmap, suggesting greater dynamic properties of chromatin in pluripotent cells (Figures 6A and 6C). Our findings strengthen the concept of chromatin plasticity in pluripotent cells (Meshorer and Misteli, 2006; Ricci et al., 2015).

DISCUSSION

In the present study, we not only revealed chromatin structures at high resolution in live cells but also their dynamic aspects, which can regulate chromatin accessibility in a manner highly related to genome function and which were not explored previously (e.g., Ricci et al., 2015; Boettiger et al., 2016). We demonstrated that nucleosomes form compact domains and that their constituent nucleosomes move coherently (Figure 7A). This suggests that chromatin domains are condensed structures like "liquid drops" rather than loose bundles of fibers or extended loops (Figure 7A; Maeshima et al., 2015). The average size of our domain structures (Figure 7A) seems to be much larger than that of heterogeneous groups of nucleosomes ("clutches" or "nanodomains"), which were revealed by Ricci et al. (2015) using higher-resolution imaging mainly in

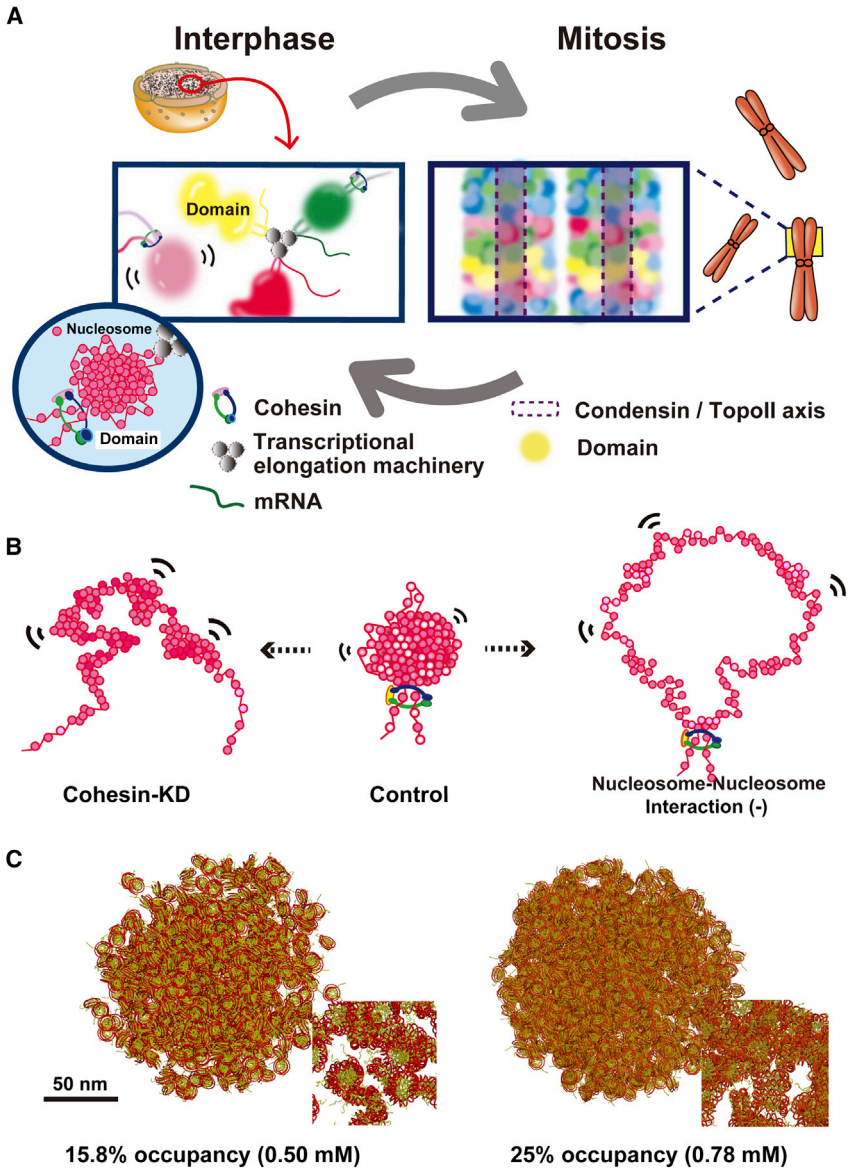

Figure 7. Chromatin Domain Structure Model

(A) Summary. In interphase (left), various compact domains are formed by cohesin and other factors, including nucleosome-nucleosome interactions. Cohesin folds the domain itself (enlarged domain in the circle), possibly via loop formation. Some chromatin domains are stabilized by transcriptional elongation machinery (gray spheres). Release of cohesin and transcriptional machinery increase domain dynamics. During mitosis, the chromatin domains are assembled, presumably by condensin (and topoisomerase IIα) and other forces, to obtain a rod-like shape.

(B) A simplified model of the effects in cohesin-KD (left) and TSA-treated (right) domains. In the cohesin-KD domain, global folding of nucleosome fibers is missing, whereas local nucleosome-nucleosome interactions are impaired in the TSA-treated domain.

(C) An "in silico domain" model. The compact domains are composed of 646 (left, corresponding to 0.50 mM) and 1,000 (right, 0.78 mM) nucleosomes in the domains with a diameter of 160 nm. The nucleosomes were randomly packed in the domains. Note that these are highly simplified models and have no linker DNAs, linker histones, or other chromatin proteins.

methanol/ethanol-fixed mammalian cells. Ricci et al. (2015) might focus on substructures of the domains.

The compact domains are organized by a combination of factors, including cohesin and nucleosome-nucleosome interactions. Because it was recently reported that the nucleosome-nucleosome interaction is quite weak (~−1.6 kcal/mol) (Funke et al., 2016), the activity of other factors, such as cohesin, could bring the nucleosome fibers together to form the compact domain (Figure 7B). This compact structure also reminded us of the large chromatin structures formed in vitro in a salt-dependent manner (Hansen, 2002; Maeshima et al., 2016b), which is consistent with the finding that the domain structures are sensitive to osmotic pressure changes related to intracellular cationic conditions (Figure 4D; Figure S5C). Notably, the compact feature of the domains can provide higher-order regulation of various DNA transaction reactions because the domains likely hinder the accessibility of protein complexes mediating the reactions to the inner core of chromatin domains (Maeshima et al., 2015).

It would be intriguing to estimate how many nucleosomes are included in the observed compact domains and to compare them with TADs and contact domains. If we assume that nucleosomes are 10-nm-diameter spheres, and that the spheres occupy 25% of the space in the domains (corresponding to 0.78 mM), FA-fixed domains with a peak diameter of 160 nm (Figure 1H) are estimated to contain 1,000 nucleosomes, covering an ~200-kb genomic region (Figure 7C). An occupancy of 15.8% in the domain (0.50 mM) should contain 646 nucleosomes, covering an ~130-kb genomic region (Figure 7C). These estimated genomic sizes in the domain are in good agreement with that of contact domains recently identified by Rao et al. (2014) (median size, ~185 kb) and may be smaller than TADs (average size, ~800 kb) (Dekker and Heard, 2015). The key role of cohesin in TAD formation (Sofueva et al., 2013; Zuin et al., 2014a) is also true for the domains observed in our study using live cells. On the other hand, although the Hi-C method did not detect notable TAD structures in mitotic chromosomes (Naumova et al., 2013), we found that they have chromatin domain structures (Figures 5C–5F; Figures S6B and S6C). In addition, although TAD structures can be observed in mouse ESCs (Nora et al., 2012), our domains are less prominent (Figure 6A), consistent with the reportedly more open structures in ESCs

(Ricci et al., 2015). Taken together, the observed domains seem to share some, but not all, of the properties of TADs or contact domains.

The domain dynamics seemed to be temperature-dependent, and temperature appeared to be the parameter that most affected domain dynamics (Figure 4E). These observations suggested that Brownian motion essentially drives the domain dynamics. On the other hand, although ATP depletion (Figure S5F) slightly decreased the domain dynamics (Figure 4E), we could not conclude that the movement was energy-dependent because chromatin condensation was also observed simultaneously (Figure 4D; Figure S5C), probably due to the reported rapid rise in Ca^{2+} upon ATP depletion (Martin et al., 2007). Systematic KD analyses of ATP-dependent chromatin proteins, such as remodelers, will provide insight into this issue.

Interestingly, the domain dynamics were increased by transcription inhibition (Figure 4B). This was the opposite of what we expected. During transcriptional elongation, some domains appear to be stabilized by the RNA Pol II elongation machinery (Figure 7A). This finding is in agreement with a previous report that a specific genomic locus was less dynamic when actively transcribed (Ochiai et al., 2015) and could also be compatible with the transcription factory model (Papantonis and Cook, 2013) or the 1-Mb domain/interchromatin domain model (Markaki et al., 2010).

Our observation of chromatin domain structures in mitotic chromosomes (Figure 7A) is consistent with the finding that DNA replication domains are retained stably during the cell cycle, including during mitosis (Albiez et al., 2006; Manders et al., 1999), and could also be compatible with other proposed large-scale structures such as the chromonema fiber (Kireeva et al., 2004). The retention of chromatin domains throughout the cell cycle provides further advantages for genome functions. First, the chromatin domains can function as "building blocks" of chromosomes, and chromosome assembly and disassembly processes become smoother, presumably with involvement of condensin, topoisomerase IIα, and other factors (Hirano, 2012; Liang et al., 2015; Ohta et al., 2011; Thadani et al., 2012; Figure 7A). Second, the memories of epigenetic markers in these building blocks could be retained easily throughout the cell cycle.

STAR★METHODS

Detailed methods are provided in the online version of this paper and include the following:

- KEY RESOURCES TABLE
- EXPERIMENTAL MODEL AND SUBJECT DETAILS
  - Cell Culture
- METHOD DETAILS
  - PALM imaging
  - Plasmid construction
  - Isolation of stable cell lines
  - Chemical treatment
  - Cell cycle synchronization
  - Flow cytometry
  - Conventional and correlative immunostaining
  - RNA interference
  - Biochemical fractionation of nuclei from cells expressing H2B-PA-mCherry
  - EU and EdU labeling
  - HaloTag labeling
  - Labeling of DNA replication domains
  - Intracellular ATP measurement based on luciferase activity
- QUANTIFICATION AND STATISTICAL ANALYSIS
  - Data analysis for PALM imaging and single nucleosome tracking
  - Clustering analyses of nucleosomes in PALM images
  - Analysis of coherent movement of nucleosomes and replication foci
  - Analysis of nuclear volume
  - Computer simulation of L-function plots for condensation and decondensation of chromatin domains
  - Computational modeling of a chromatin domain
- DATA AND SOFTWARE AVAILABILITY

SUPPLEMENTAL INFORMATION

Supplemental Information includes seven figures and three movies and can be found with this article online at http://dx.doi.org/10.1016/j.molcel.2017.06.018.

AUTHOR CONTRIBUTIONS

T. Nozaki and K.M. designed the project. T. Nozaki performed most of the PALM imaging, clustering analyses, and immunostaining. R.I., M. Tanbo, and R.N. performed some PALM imaging and analyses. T. Nozaki, M. Tanbo, R.I., R.N., and S.T. performed DNA construction and stable cell establishment. S.T. contributed to immunoblotting and illustrations. T.T. and T. Nagai contributed to the initial PALM imaging. Y.J. performed the computational modeling analysis. M.T.K. contributed to the creation of RAD21-AID cells. K.S.W. contributed some materials. M. Tomita, T.T., K.H., K.S.W., Y.O., and T. Nagai provided some essential advice. K.M. and T. Nozaki wrote the manuscript with input from all other authors.

ACKNOWLEDGMENTS

We are grateful to Dr. D. Hudson, Dr. S. Shinkai, Dr. Y. Hiromi, Dr. N. Kleckner, and Dr. M. Kurusu for critical reading of this manuscript. We thank Dr. H. Kimura, Dr. J. Takeda, Dr. K. Horie, Dr. I. Hiratani, and Dr. T. Tachibana for providing materials and suggestions and Dr. I. Sase (Nikon) for valuable help and advice regarding the microscopy system. We also thank Dr. T. Cremer, Dr. J. Dekker, Dr. A. Belmont, and the Maeshima lab members for helpful discussions and support. This work was supported by MEXT (23115005) and JSPS (16H04746) grants and JST CREST grant JPMJCR15G2.

Received: February 4, 2017
Revised: April 17, 2017
Accepted: June 16, 2017
Published: July 13, 2017

REFERENCES

Abdi, H. (2007). RV coefficient and congruence coefficient. In Encyclopedia of Measurement and Statistics, N.J. Salkind, ed. (SAGE Publications Inc), pp. 849–853.

Albiez, H., Cremer, M., Tiberi, C., Vecchio, L., Schermelleh, L., Dittrich, S., Küpper, K., Joffe, B., Thormeyer, T., von Hase, J., et al. (2006). Chromatin

domains and the interchromatin compartment form structurally defined and functionally interacting nuclear networks. Chromosome Res. *14*, 707–733.

Baddeley, D., Chagin, V.O., Schermelleh, L., Martin, S., Pombo, A., Carlton, P.M., Gahl, A., Domaing, P., Birk, U., Leonhardt, H., et al. (2010). Measurement of replication structures at the nanometer scale using super-resolution light microscopy. Nucleic Acids Res. *38*, e8.

Betzig, E., Patterson, G.H., Sougrat, R., Lindwasser, O.W., Olenych, S., Bonifacino, J.S., Davidson, M.W., Lippincott-Schwartz, J., and Hess, H.F. (2006). Imaging intracellular fluorescent proteins at nanometer resolution. Science *313*, 1642–1645.

Bickmore, W.A. (2013). The spatial organization of the human genome. Annu. Rev. Genomics Hum. Genet. *14*, 67–84.

Boettiger, A.N., Bintu, B., Moffitt, J.R., Wang, S., Beliveau, B.J., Fudenberg, G., Imakaev, M., Mirny, L.A., Wu, C.T., and Zhuang, X. (2016). Super-resolution imaging reveals distinct chromatin folding for different epigenetic states. Nature *529*, 418–422.

Bohn, M., Diesinger, P., Kaufmann, R., Weiland, Y., Müller, P., Gunkel, M., von Ketteler, A., Lemmer, P., Hausmann, M., Heermann, D.W., and Cremer, C. (2010). Localization microscopy reveals expression-dependent parameters of chromatin nanostructure. Biophys. J. *99*, 1358–1367.

Cardoso, M.C., Schneider, K., Martin, R.M., and Leonhardt, H. (2012). Structure, function and dynamics of nuclear subcompartments. Curr. Opin. Cell Biol. *24*, 79–85.

Chen, C., Lim, H.H., Shi, J., Tamura, S., Maeshima, K., Surana, U., and Gan, L. (2016). Budding yeast chromatin is dispersed in a crowded nucleoplasm in vivo. Mol. Biol. Cell *27*, 3357–3368.

Cheng, T.M., Heeger, S., Chaleil, R.A., Matthews, N., Stewart, A., Wright, J., Lim, C., Bates, P.A., and Uhlmann, F. (2015). A simple biophysical model emulates budding yeast chromosome condensation. eLife *4*, e05565.

Cseresnyes, Z., Schwarz, U., and Green, C.M. (2009). Analysis of replication factories in human cells by super-resolution light microscopy. BMC Cell Biol. *10*, 88.

Dekker, J., and Heard, E. (2015). Structural and functional diversity of Topologically Associating Domains. FEBS Lett. *589* (20 Pt A), 2877–2884.

Dixon, J.R., Selvaraj, S., Yue, F., Kim, A., Li, Y., Shen, Y., Hu, M., Liu, J.S., and Ren, B. (2012). Topological domains in mammalian genomes identified by analysis of chromatin interactions. Nature *485*, 376–380.

Eltsov, M., Maclellan, K.M., Maeshima, K., Frangakis, A.S., and Dubochet, J. (2008). Analysis of cryo-electron microscopy images does not support the existence of 30-nm chromatin fibers in mitotic chromosomes in situ. Proc. Natl. Acad. Sci. USA *105*, 19732–19737.

Funke, J.J., Ketterer, P., Lieleg, C., Schunter, S., Korber, P., and Dietz, H. (2016). Uncovering the forces between nucleosomes using DNA origami. Sci. Adv. *2*, e1600974.

Fussner, E., Strauss, M., Djuric, U., Li, R., Ahmed, K., Hart, M., Ellis, J., and Bazett-Jones, D.P. (2012). Open and closed domains in the mouse genome are configured as 10-nm chromatin fibres. EMBO Rep. *13*, 992–996.

Görisch, S.M., Wachsmuth, M., Tóth, K.F., Lichter, P., and Rippe, K. (2005). Histone acetylation increases chromatin accessibility. J. Cell Sci. *118*, 5825–5834.

Hansen, J.C. (2002). Conformational dynamics of the chromatin fiber in solution: determinants, mechanisms, and functions. Annu. Rev. Biophys. Biomol. Struct. *31*, 361–392.

Hihara, S., Pack, C.G., Kaizu, K., Tani, T., Hanafusa, T., Nozaki, T., Takemoto, S., Yoshimi, T., Yokota, H., Imamoto, N., et al. (2012). Local nucleosome dynamics facilitate chromatin accessibility in living mammalian cells. Cell Rep. *2*, 1645–1656.

Hirano, T. (2012). Condensins: universal organizers of chromosomes with diverse functions. Genes Dev. *26*, 1659–1678.

Hsieh, T.H., Weiner, A., Lajoie, B., Dekker, J., Friedman, N., and Rando, O.J. (2015). Mapping Nucleosome resolution chromosome folding in yeast by micro-C. Cell *162*, 108–119.

Hübner, M.R., Eckersley-Maslin, M.A., and Spector, D.L. (2013). Chromatin organization and transcriptional regulation. Curr. Opin. Genet. Dev. *23*, 89–95.

Iemura, K., and Tanaka, K. (2015). Chromokinesin Kid and kinetochore kinesin CENP-E differentially support chromosome congression without end-on attachment to microtubules. Nat. Commun. *6*, 6447.

Jackson, D.A., and Pombo, A. (1998). Replicon clusters are stable units of chromosome structure: evidence that nuclear organization contributes to the efficient activation and propagation of S phase in human cells. J. Cell Biol. *140*, 1285–1295.

Jaqaman, K., Loerke, D., Mettlen, M., Kuwata, H., Grinstein, S., Schmid, S.L., and Danuser, G. (2008). Robust single-particle tracking in live-cell time-lapse sequences. Nat. Methods *5*, 695–702.

Kalashnikova, A.A., Porter-Goff, M.E., Muthurajan, U.M., Luger, K., and Hansen, J.C. (2013). The role of the nucleosome acidic patch in modulating higher order chromatin structure. J. R. Soc. Interface *10*, 20121022.

Kimura, H., and Cook, P.R. (2001). Kinetics of core histones in living human cells: little exchange of H3 and H4 and some rapid exchange of H2B. J. Cell Biol. *153*, 1341–1353.

Kimura, H., Sugaya, K., and Cook, P.R. (2002). The transcription cycle of RNA polymerase II in living cells. J. Cell Biol. *159*, 777–782.

Kireeva, N., Lakonishok, M., Kireev, I., Hirano, T., and Belmont, A.S. (2004). Visualization of early chromosome condensation: a hierarchical folding, axial glue model of chromosome structure. J. Cell Biol. *166*, 775–785.

Kwak, H., and Lis, J.T. (2013). Control of transcriptional elongation. Annu. Rev. Genet. *47*, 483–508.

Lemaître, C., and Bickmore, W.A. (2015). Chromatin at the nuclear periphery and the regulation of genome functions. Histochem. Cell Biol. *144*, 111–122.

Liang, Z., Zickler, D., Prentiss, M., Chang, F.S., Witz, G., Maeshima, K., and Kleckner, N. (2015). Chromosomes progress to metaphase in multiple discrete steps via global compaction/expansion cycles. Cell *161*, 1124–1137.

Luger, K., Mäder, A.W., Richmond, R.K., Sargent, D.F., and Richmond, T.J. (1997). Crystal structure of the nucleosome core particle at 2.8 A resolution. Nature *389*, 251–260.

Maeshima, K., Yahata, K., Sasaki, Y., Nakatomi, R., Tachibana, T., Hashikawa, T., Imamoto, F., and Imamoto, N. (2006). Cell-cycle-dependent dynamics of nuclear pores: pore-free islands and lamins. J. Cell Sci. *119*, 4442–4451.

Maeshima, K., Imai, R., Hikima, T., and Joti, Y. (2014). Chromatin structure revealed by X-ray scattering analysis and computational modeling. Methods *70*, 154–161.

Maeshima, K., Kaizu, K., Tamura, S., Nozaki, T., Kokubo, T., and Takahashi, K. (2015). The physical size of transcription factors is key to transcriptional regulation in the chromatin domains. J. Phys. Condens. Matter *27*, 064116.

Maeshima, K., Ide, S., Hibino, K., and Sasai, M. (2016a). Liquid-like behavior of chromatin. Curr. Opin. Genet. Dev. *37*, 36–45.

Maeshima, K., Rogge, R., Tamura, S., Joti, Y., Hikima, T., Szerlong, H., Krause, C., Herman, J., Seidel, E., DeLuca, J., et al. (2016b). Nucleosomal arrays self-assemble into supramolecular globular structures lacking 30-nm fibers. EMBO J. *35*, 1115–1132.

Manders, E.M., Kimura, H., and Cook, P.R. (1999). Direct imaging of DNA in living cells reveals the dynamics of chromosome formation. J. Cell Biol. *144*, 813–821.

Manley, S., Gillette, J.M., Patterson, G.H., Shroff, H., Hess, H.F., Betzig, E., and Lippincott-Schwartz, J. (2008). High-density mapping of single-molecule trajectories with photoactivated localization microscopy. Nat. Methods *5*, 155–157.

Markaki, Y., Gunkel, M., Schermelleh, L., Beichmanis, S., Neumann, J., Heidemann, M., Leonhardt, H., Eick, D., Cremer, C., and Cremer, T. (2010). Functional nuclear organization of transcription and DNA replication: a topographical marriage between chromatin domains and the interchromatin compartment. Cold Spring Harb. Symp. Quant. Biol. *75*, 475–492.

Martin, R.M., Görisch, S.M., Leonhardt, H., and Cardoso, M.C. (2007). An unexpected link between energy metabolism, calcium, chromatin condensation and cell cycle. Cell Cycle *6*, 2422–2424.

Meshorer, E., and Misteli, T. (2006). Chromatin in pluripotent embryonic stem cells and differentiation. Nat. Rev. Mol. Cell Biol. *7*, 540–546.

Nasmyth, K., and Haering, C.H. (2005). The structure and function of SMC and kleisin complexes. Annu. Rev. Biochem. *74*, 595–648.

Natsume, T., Kiyomitsu, T., Saga, Y., and Kanemaki, M.T. (2016). Rapid protein depletion in human cells by auxin-inducible degron tagging with short homology donors. Cell Rep. *15*, 210–218.

Naumova, N., Imakaev, M., Fudenberg, G., Zhan, Y., Lajoie, B.R., Mirny, L.A., and Dekker, J. (2013). Organization of the mitotic chromosome. Science *342*, 948–953.

Nora, E.P., Lajoie, B.R., Schulz, E.G., Giorgetti, L., Okamoto, I., Servant, N., Piolot, T., van Berkum, N.L., Meisig, J., Sedat, J., et al. (2012). Spatial partitioning of the regulatory landscape of the X-inactivation centre. Nature *485*, 381–385.

Nozaki, T., Kaizu, K., Pack, C.G., Tamura, S., Tani, T., Hihara, S., Nagai, T., Takahashi, K., and Maeshima, K. (2013). Flexible and dynamic nucleosome fiber in living mammalian cells. Nucleus *4*, 349–356.

O'Keefe, R.T., Henderson, S.C., and Spector, D.L. (1992). Dynamic organization of DNA replication in mammalian cell nuclei: spatially and temporally defined replication of chromosome-specific alpha-satellite DNA sequences. J. Cell Biol. *116*, 1095–1110.

Ochiai, H., Sugawara, T., and Yamamoto, T. (2015). Simultaneous live imaging of the transcription and nuclear position of specific genes. Nucleic Acids Res. *43*, e127.

Ohta, S., Wood, L., Bukowski-Wills, J.C., Rappsilber, J., and Earnshaw, W.C. (2011). Building mitotic chromosomes. Curr. Opin. Cell Biol. *23*, 114–121.

Ono, T., Yamashita, D., and Hirano, T. (2013). Condensin II initiates sister chromatid resolution during S phase. J. Cell Biol. *200*, 429–441.

Ozer, G., Luque, A., and Schlick, T. (2015). The chromatin fiber: multiscale problems and approaches. Curr. Opin. Struct. Biol. *31*, 124–139.

Papantonis, A., and Cook, P.R. (2013). Transcription factories: genome organization and gene regulation. Chem. Rev. *113*, 8683–8705.

Rao, S.S., Huntley, M.H., Durand, N.C., Stamenova, E.K., Bochkov, I.D., Robinson, J.T., Sanborn, A.L., Machol, I., Omer, A.D., Lander, E.S., and Aiden, E.L. (2014). A 3D map of the human genome at kilobase resolution reveals principles of chromatin looping. Cell *159*, 1665–1680.

Ricci, M.A., Manzo, C., García-Parajo, M.F., Lakadamyali, M., and Cosma, M.P. (2015). Chromatin fibers are formed by heterogeneous groups of nucleosomes in vivo. Cell *160*, 1145–1158.

Rust, M.J., Bates, M., and Zhuang, X. (2006). Sub-diffraction-limit imaging by stochastic optical reconstruction microscopy (STORM). Nat. Methods *3*, 793–795.

Ryba, T., Hiratani, I., Lu, J., Itoh, M., Kulik, M., Zhang, J., Schulz, T.C., Robins, A.J., Dalton, S., and Gilbert, D.M. (2010). Evolutionarily conserved replication timing profiles predict long-range chromatin interactions and distinguish closely related cell types. Genome Res. *20*, 761–770.

Sanborn, A.L., Rao, S.S., Huang, S.C., Durand, N.C., Huntley, M.H., Jewett, A.I., Bochkov, I.D., Chinnappan, D., Cutkosky, A., Li, J., et al. (2015). Chromatin extrusion explains key features of loop and domain formation in wild-type and engineered genomes. Proc. Natl. Acad. Sci. USA *112*, E6456–E6465.

Sexton, T., Yaffe, E., Kenigsberg, E., Bantignies, F., Leblanc, B., Hoichman, M., Parrinello, H., Tanay, A., and Cavalli, G. (2012). Three-dimensional folding and functional organization principles of the *Drosophila* genome. Cell *148*, 458–472.

Shinkai, S., Nozaki, T., Maeshima, K., and Togashi, Y. (2016). Dynamic nucleosome movement provides structural information of topological chromatin domains in living human cells. PLoS Comput. Biol. *12*, e1005136.

Shintomi, K., and Hirano, T. (2010). Sister chromatid resolution: a cohesin releasing network and beyond. Chromosoma *119*, 459–467.

Sofueva, S., Yaffe, E., Chan, W.C., Georgopoulou, D., Vietri Rudan, M., Mira-Bontenbal, H., Pollard, S.M., Schroth, G.P., Tanay, A., and Hadjur, S. (2013). Cohesin-mediated interactions organize chromosomal domain architecture. EMBO J. *32*, 3119–3129.

Stasevich, T.J., Sato, Y., Nozaki, N., and Kimura, H. (2014). Quantifying histone and RNA polymerase II post-translational modification dynamics in mother and daughter cells. Methods *70*, 77–88.

Subach, F.V., Patterson, G.H., Manley, S., Gillette, J.M., Lippincott-Schwartz, J., and Verkhusha, V.V. (2009). Photoactivatable mCherry for high-resolution two-color fluorescence microscopy. Nat. Methods *6*, 153–159.

Thadani, R., Uhlmann, F., and Heeger, S. (2012). Condensin, chromatin crossbarring and chromosome condensation. Curr. Biol. *22*, R1012–R1021.

Tokunaga, M., Imamoto, N., and Sakata-Sogawa, K. (2008). Highly inclined thin illumination enables clear single-molecule imaging in cells. Nat. Methods *5*, 159–161.

Uhlmann, F. (2016). SMC complexes: from DNA to chromosomes. Nat. Rev. Mol. Cell Biol. *17*, 399–412.

Wendt, K.S., Yoshida, K., Itoh, T., Bando, M., Koch, B., Schirghuber, E., Tsutsumi, S., Nagae, G., Ishihara, K., Mishiro, T., et al. (2008). Cohesin mediates transcriptional insulation by CCCTC-binding factor. Nature *451*, 796–801.

Zuin, J., Dixon, J.R., van der Reijden, M.I., Ye, Z., Kolovos, P., Brouwer, R.W., van de Corput, M.P., van de Werken, H.J., Knoch, T.A., van Ijken, W.F., et al. (2014a). Cohesin and CTCF differentially affect chromatin architecture and gene expression in human cells. Proc. Natl. Acad. Sci. U.S.A *111*, 996–1001.

Zuin, J., Franke, V., van Ijcken, W.F., van der Sloot, A., Krantz, I.D., van der Reijden, M.I., Nakato, R., Lenhard, B., and Wendt, K.S. (2014b). A cohesin-independent role for NIPBL at promoters provides insights in CdLS. PLoS Genet. *10*, e1004153.

STAR★METHODS

KEY RESOURCES TABLE

REAGENT or RESOURCE	SOURCE	IDENTIFIER
Antibodies		
Mouse monoclonal anti-RAD21	Millipore	Cat#05-908
Rabbit polyclonal anti-CTCF	Millipore	Cat#07-729
Mouse monoclonal anti-NIPBL	Santa Cruz	Cat#sc-374625
Rat monoclonal anti-CAP-H2	Sigma-Aldrich	Cat#SAB4200655-100UL
Rabbit polyclonal anti-Sox2	Abcam	Cat#ab97959
Mouse monoclonal anti-H3K9me3	Hiroshi Kimura Lab (Tokyo Institute of Technology)	N/A
Mouse monoclonal anti-Polymerase II Ser 5 ph	Hiroshi Kimura Lab (Tokyo Institute of Technology)	N/A
Rabbit polyclonal anti-Histone H2B	upstate	Cat#07-371
Rabbit polyclonal anti-RFP	MBL	Cat#PM005
Chemicals, Peptides, and Recombinant Proteins		
Formaldehyde solution	Wako	Cat#064-00406
Trichostatin A (TSA)	Wako	Cat#203-17561
Sodium azide	Sigma-Aldrich	Cat#S2002-25G
2-Deoxy-D-glucose	Sigma-Aldrich	Cat#D8375-1G
5,6-Dichloro-1-beta-D-ribofuranosylbenzimidazole	Sigma-Aldrich	Cat#D1916-10MG
3-indoleacetic acid	Nacalai	Cat#19119-61
Nocodazole	Wako	Cat#140-08531
Hoechst 33342	Dojindo	Cat#H342
DAPI	Roche	Cat#10236276001
Lipofectamine RNAiMAX Transfection Reagent	Invitrogen	Cat#13778-075
HaloTag R110 Direct Ligand	Promega	Cat#G3221
Cy3-dCTP	GE	Cat#PA53021
Poly-L-lysine	Sigma-Aldrich	Cat#P1524-500MG
Blasticidin S Hydrochloride	Wako	Cat#029-18701
G418	ENZ	Cat#ALX-380-013-G001
FxCycle Far Red Stain	Invitrogen	Cat#F10348
TetraSpeck beads (0.1μm)	Molecular Probes	Cat#T7279
Di(N-succinimidyl) glutarate (DSG)	Sigma-Aldrich	Cat#80424-50MG-F
Critical Commercial Assays		
Effectene Transfection Reagent	QIAGEN	Cat#301425
Click-iT EdU Alexa Fluor 488 Flow cytometry assay Kit	Invitrogen	Cat#C10425
Click-iT RNA Alexa Fluor 594 Imaging Kit	Invitrogen	Cat#C10330
Cell ATP Assay Regent	Toyo B	Cat#300–15363
Hyglomycin B	Invitrogen	Cat#10687010
Experimental Models: Cell Lines		
Human: HeLaS3	(Maeshima et al., 2006)	N/A
Mouse: Embryonic stem cell (E14Tg2a)	Ichiro Hiratani Lab	N/A
Indian Muntjac: DM	Hihara et al., 2012	N/A
Human: HCT116,RAD21-mAID-mClover,OsTIR1 clone12	Natsume et al., 2016	N/A

(*Continued on next page*)

Continued

REAGENT or RESOURCE	SOURCE	IDENTIFIER
Oligonucleotides		
Primer: BamHI-PAmCherry-Fw: CGCGGATCCACCGGTCG CCACCATGGTGAGCAAGGG	This paper	N/A
Primer: NotI-PAmCherry-Rv: AAGGAAAAAAGCGGCCGCTT ACTTGTACAGCTCGTCCA	This paper	N/A
Primer: mRFP-H2B-Nh21-Fw: CTAGCTAGCATGCCAGAG CCAGCGAAGTCTG	This paper	N/A
Primer: Halotag-NotI-Fw(1st): TGGAGGCTCAGGAGGTGGC GGGTCTGGATCCGAAATCGGTACTG	This paper	N/A
Primer: Halotag NotI-Rv: ATAAGAATGCGGCCGCTTAAC CGGAAATCTCCAGAG	This paper	N/A
Primer: Halotag-NotI-Fw(2nd): ATAAGAATGCGGCCGCTA AGTGGCGGTGGAGGCTCAGGAGGTGGCG	This paper	N/A
Primer: EcoRV-EF1α-Fw: AAAGATATCGGTCTTGAAAGG AGTGCCTCG	This paper	N/A
Primer: EcoRV-BGH polyA-Rv: AAAGATATCAAGCCATA GAGCCCACCGCAT	This paper	N/A
Primer: XhoI-H2B-Fw: CCGCTCGAGATGCCAGAGCCA GCGAAGTC	This paper	N/A
Primer: XhoI-PAmCherry-Rv: CCGCTCGAGTTACTTGTA CAGCTCGTCCATGCCG	This paper	N/A
siRNA control: Low GC content oligo	Invitrogen	Cat#45-2002
siRNA targeting sequence NIPBL:	(Zuin et al., 2014b)	N/A
sense: 5′-GCAUCGGUAUCAAGUCCCAUUtt-3′		
antisense: 5′-AAUGGGACUUGAUACCGAUGCtt-3′		
siRNA targeting sequence RAD21	(Wendt et al., 2008)	N/A
sense: 5′-CAGCUUGAAUCAGAGUAGAGUGGAA-3′		
antisense: 5′-UUCCACUCUACUCUGAUUCAAGCUG-3′		
siRNA targeting sequence CTCF	(Wendt et al., 2008)	N/A
sense:5′-GCGCUCUAAGAAAGAAGAUUCCUCU-3′ antisense:5′-AGAGGAAUCUUCUUUCUUAGAGCGC-3′		
siRNA targeting sequence CAP-H2	(Ono et al., 2013)	N/A
sense: 5′-CAGGCCCUUGAUUUCAUCUCUGGAA-3′		
antisense: 5′-UUCCAGAGAUGAAAUCAAGGGCCUG-3′		
siRNA targeting sequence CAP-G2	(Ono et al., 2013)	N/A
sense: 5′-AGCCCUACUGGAAUGUGUUAUUAUA-3′		
antisense- 5′-UAUAAUAACACAUUCCAGUAGGGCU-3′		
Recombinant DNA		
pPAmCherry-N1	Clontech	Cat#632584
pH2B-PA-GFP	EUROSCARF	Cat#P30499
pEF5/FRT/V5-DEST Gateway Vector	Invitrogen	Cat#V602020
pFC14A HaloTag CMV Flexi Vector	Promega	Cat#G965A
pEF1α-H2B-PAmCherry-FRT	This paper	N/A
pEF1α-H2B-HaloTag-FRT	This paper	N/A
pPB-EF1α-H2B-PA-mCherry-PGKneo	This paper	N/A
pPB-CAG-IB-H2B-PA-mCherry	This paper	N/A
pPB-PGKneo	Sanger Institute (MTA) Junji Takeda Lab	N/A

(*Continued on next page*)

Continued		
REAGENT or RESOURCE	SOURCE	IDENTIFIER
pPB-CAG-IB	Sanger Institute (MTA) Junji Takeda Lab	N/A
pCMV-hyPBase	Sanger Institute (MTA)	N/A
Software and Algorithms		
u-track	(Jaqaman et al., 2008)	http://www.utsouthwestern.edu/labs/danuser/software/#utrack_anc
KaleidaGraph	Synergy Software	http://www.synergy.com/wordpress_650164087/
Fiji	Fiji	http://fiji.sc/
ImageJ	ImageJ	https://imagej.nih.gov/ij/
TrackMate	ImageJ	https://imagej.net/TrackMate
Particle Tracker	ImageJ	http://imagej.net/Particle_Tracker
R	R	https://www.r-project.org/
vec2dtransf	CRAN	https://cran.r-project.org/web/packages/vec2dtransf/index.html
MetaMorph	Molecular Device	https://www.moleculardevices.com/systems/metamorph-research-imaging/metamorph-microscopy-automation-and-image-analysis-software
Deposited Data		
Raw imaging data	This paper	Mendeley data: http://dx.doi.org/10.17632/wr6zsbmshp.1

EXPERIMENTAL MODEL AND SUBJECT DETAILS

Cell Culture

The cells were cultured in Dulbecco's modified Eagle's medium (DMEM) supplemented with 10% (HeLa) or 15% (DM) fetal bovine serum (FBS) at 37°C in 5% CO_2. HCT116 cells were cultured in McCoy's 5A (Modified) medium supplemented with 10% FBS and 2 mM L-glutamine. E14Tg2a ESCs were cultured in Glasgow minimum essential medium (GMEM) supplemented with 10% FBS, 1% non-essential amino acids, 1 mM sodium pyruvate solution, 2 mM L-glutamine, 1 mM 2-mercaptoethanol, and 100 U/mL LIF. For the LIF(–) condition, ESCs were cultured for 5 days after withdrawal of LIF.

METHOD DETAILS

PALM imaging

PALM imaging was performed using the inverted Nikon Eclipse Ti microscope with a 100 mW Sapphire 561 nm laser (Coherent) and sCMOS ORCA-Flash 4.0 camera (Hamamatsu Photonics). Cells were exposed to the excitation laser through an objective lens (100 × PlanApo TIRF, NA 1.49; Nikon). The images were taken using an oblique illumination system with a TIRF unit (Nikon) to illuminate a limited thin area in the cell nucleus. Movies of 1,000 sequential frames were acquired using MetaMorph software (Molecular Devices) in 50 ms under continuous illumination. To maintain cell culture conditions (37°C, 5% CO_2, and humidity during imaging), a live-cell chamber and GM-8000 digital gas mixer (Tokai Hit) were used. For PALM imaging, all cell types were plated onto glass-bottomed dishes (Iwaki) treated with polylysine. Before microscopy imaging, the medium was replaced with DMEM (no Phenol Red and 10% or 15% FBS). For PALM imaging of the chemically fixed interphase cells, we used DAPI LED light (Lumencor) for 50 ms to activate PA-mCherry. To measure the depth of the focal plane in the oblique illumination system, we observed H2B-PA-mCherry in fixed HeLa cells using a Piezo stage (Mad City Labs) at 50 nm/frame (z direction) without the Perfect Focus system and created the kymograph of single H2B-PA-mCherry.

Plasmid construction

Construction of pEF1α-H2B-PAmCherry-FRT was performed as follows. The PA-mCherry sequence with the addition of *Bam*HI and *Not*I sites to the ends of pPA-mCherry-N1 (Clontech) was amplified using the following primer pair: 5′-CGCGGATCCACCGGTCGC CACCATGGTGAGCAAGGG-3′ and 5′-AAGGAAAAAAGCGGCCGCTTACTTGTACAGCTCGTCCA-3′. The amplified PA-mCherry fragment was replaced with the PA-GFP region of the pH2B-PA-GFP vector (EUROSCARF, Ellenberg lab) via *Bam*HI and *Not*I sites.

The H2B-PA-mCherry sequence was then amplified using the following PCR primer pair: 5′-CTAGCTAGCATGCCAGAGCCAGC GAAGTC-3′ and 5′-AAGGAAAAAAGCGGCCGCTTACTTGTACAGCTCGTCCA-3′. This fragment was inserted into the *Eco*RV site of the pEF5/FRT/V5-DEST Gateway Vector (Invitrogen) to obtain pEF1α-H2B-PAmCherry-FRT.

Construction of pEF1α-H2B-Halotag-FRT was performed as follows. To generate a long linker sequence, the Halotag sequence on pFC14A HaloTag CMV Flexi Vector (Promega) was amplified twice, first using the primer pair 5′-TGGAGGCTCAGGAGGTGGCG GGTCTGGATCCGAAATCGGTACTG-3′ and 5′- ATAAGAATGCGGCCGCTTAACCGGAAATCTCCAGAG-3′ and again using the following primer pair with *Not*I sites added to the ends: 5′-ATAAGAATGCGGCCGCTAAGTGGCGGTGGAGGCTCAGGAGGTG GCG-3′ and 5′- ATAAGAATGCGGCCGCTTAACCGGAAATCTCCAGAG-3′. The amplified HaloTag fragment was replaced with the PA-mCherry region of the pH2B-PA-mCherry vector (described above) via *Not*I sites to create the pH2B-HaloTag vector. Similar to H2B-PA-mCherry, this fragment was amplified and inserted into the *Eco*RV site of the pEF5/FRT/V5-DEST Gateway Vector (Invitrogen) to obtain the pEF1α-H2B-HaloTag-FRT vector.

To construct pEF1α-H2B-PAmCherry in the PiggyBac vector (pPB-EF1α-H2B-PA-mCherry-PGKneo), the H2B-PA-mCherry sequence was amplified from pEF1α-H2B-PA-mCherry using the following primer pair: 5′-AAAGATATCGGTCTTGAAAGGAGTG CCTCG-3′ and 5′-AAAGATATCAAGCCATAGAGCCCACCGCAT-3′. The amplified fragment was digested by *Eco*RV and then inserted into the *Eco*RV site of the pPB-PGKneo vector.

Construction of pPB-CAG-IB-H2B-PA-mCherry was performed as follows: the H2B-PA-mCherry sequence with the addition of *Xho*I sites to the ends of pEF1α-H2B-PA-mCherry-FRT was amplified using the following primer pair: 5′- CCGCTCGAGATGCCA GAGCCAGCGAAGTC-3′ and 5′- CCGCTCGAGTTACTTGTACAGCTCGTCCATGCCG −3′. This fragment was inserted into the *Xho*I site of pPB-CAG-IB (Invitrogen) to obtain the pPB-CAG-IB-H2B-PA-mCherry vector.

Isolation of stable cell lines

To establish HeLa or DM cells stably expressing H2B-PA-mCherry, the Flp-In system (Invitrogen) was used as described previously (Hihara et al., 2012). To establish HeLa cells stably expressing H2B-HaloTag, the Flp-In system (Invitrogen) was also used. For establishment of HCT116 RAD21-mAID-mClover OsTIRI cells (Natsume et al., 2016) and ESCs stably expressing H2B-PA-mCherry, the PiggyBac transposon system was used. pPB-CAG-IB-H2B-PA-mCherry and pCMV-hyPBase were transfected into the HCT116 411 cells using Effectene Transfection Reagent (QIAGEN), and transformants were then selected using 10 μg/mL blasticidin. pPB-EF1α-H2B-PA-mCherry-PGKneo and pCMV-hyPBase were transfected into the cells using Effectene Transfection Reagent (QIAGEN), and transformants were then selected using 600 μg/mL G418.

Chemical treatment

For chemical fixation, cells were incubated in 2% FA (Wako) in 1 × HBSS for 15 min or 4mM disuccinimidyl glutarate (DSG) for 7 hr and washed with 1 × HBSS. To increase histone tail acetylation, cells were treated with 500 nM TSA (Wako) for 8 hr. For FA-fixed and TSA-treated cell imaging, cells were treated with 500 nM TSA for 3 hr and 2% FA (Wako) in 1 × HBSS for 15 min and washed with 1 × HBSS. To deplete ATP, cells were incubated in medium supplemented with 10 mM sodium azide (Sigma-Aldrich) and 50 mM 2-deoxy-glucose (Sigma-Aldrich) for 30 min. For inhibition of transcription, cells were cultured in medium supplemented with 100 μM DRB (Sigma-Aldrich) for 2 hr or 50 μg/mL DRB for 3 hr. For hypotonic treatment, cells were incubated in medium supplemented with 1 mL DMEM and 1 mL MilliQ water for 2 hr. To induce the degradation of RAD21-mAID, 500 μM indole-3-acetic acid, a natural auxin, was added to the culture medium, and cells were cultured for 1 hr before imaging.

Cell cycle synchronization

HeLa cells were synchronized with 0.08 μg/mL nocodazole (Wako) for 4 hr, and mitotic cells were harvested by shake-off. Cells were washed with PBS(–) and plated on glass-bottomed dishes with DMEM medium.

Flow cytometry

Flow cytometry (FCM) was performed to determine when the cells entered each phase of the cell cycle after release from synchronization. Mitotic cells synchronized by nocodazole were isolated by shake-off and seeded into a new culture dish. The cells were pulse-labeled for 60 min with 10 μM 5-ethynyl-2′-deoxyuridine (EdU) at 7, 12, 15, 18, and 21 hr after shake-off. Pulse-labeled cells were then trypsinized and fixed with ice-cold ethanol at 8, 13, 16, 19, and 22 hr after shake-off. After harvesting, to fluorescently label the incorporated EdU in newly synthesized DNA, Click-iT EdU Flow Cytometry Assay kits (Invitrogen) were used. To label the DNA, cells were also stained with FxCycle Far Red Stain (Invitrogen). FCM analysis was performed using a JSAN cell sorter (Bay Bioscience) with a logarithmic FL1-A channel for EdU detection and a linear FL5-A setting for FxCycle Far Red Stain. The cells with abnormal shapes or multiple nuclei were eliminated by forward/sideward scatter gating. Analysis was performed using Flowlogic software. For each analysis, we started with $\sim 10^6$ cells, and $\sim 10^4$ cells of the flow cytometer results were plotted.

Conventional and correlative immunostaining

Immunostaining was performed as described previously (Hihara et al., 2012; Maeshima et al., 2006). Cells were fixed in 2% FA (Wako) or cold methanol. Primary antibodies were mouse anti-RAD21 (05-908; Millipore), rabbit anti-CTCF (07-729; Millipore), mouse anti-NIPBL (sc-374625; Santa Cruz), rat anti-CAP-H2 (SAB4200655-100UL; Sigma-Aldrich), rabbit anti-Sox2 (ab97959; Abcam), mouse

anti-H3K9me3 (a generous gift from Prof. Hiroshi Kimura), and mouse anti-polymerase II Ser5ph (a generous gift from Prof. Hiroshi Kimura). Images were obtained using a DeltaVision microscopy imaging system (Applied Precision) or Nikon Eclipse Ti microscope. For DNA staining in live cells, Hoechst 33342 (500 ng/mL) (Dojindo) was added to the cells for 30 min followed by washing with PBS(–). For DNA staining in fixed cells, DAPI (500 ng/mL) was added to the cells for 5 min followed by washing with PBS(–).

For correlative immunostaining, cells were plated on glass-bottomed dishes containing a grid (Matsunami) coated with polylysine. After live-cell PALM imaging, cells were fixed in 2% FA (Wako), followed by conventional immunostaining. After staining, the same cells were sought based on the grid coordinates, and images were obtained using a DeltaVision microscopy imaging system or Nikon Eclipse Ti microscope.

RNA interference

Transfection of siRNA was performed using Lipofectamine RNAiMAX (Invitrogen) according to the manufacturer's instructions. The following siRNA oligos were used as reported previously: RAD21 (Wendt et al., 2008), CTCF (Wendt et al., 2008), CAPH2 (Ono et al., 2013), CAPG2 (Ono et al., 2013), and NIPBL (Zuin et al., 2014b). An oligo with low GC content (45-2002; Invitrogen) was used as a control. For double treatment with RAD21-KD and TSA, cells were cultured for 48 hr after RAD21 siRNA transfection and then treated with TSA (500 nM) for 4 hr.

Biochemical fractionation of nuclei from cells expressing H2B-PA-mCherry

Nuclei were isolated from HeLa cells expressing H2B-PA-mCherry as described previously (Maeshima et al., 2016b). Briefly Collected cells were suspended in nuclei isolation buffer (3.75 mM Tris-HCl [pH 7.5], 20 mM KCl, 0.5 mM EDTA, 0.05 mM spermine, 0.125 mM spermidine, 1 μg/ml Aprotinin, 0.1 mM phenylmethylsulphonyl fluoride [PMSF]) and centrifuged at 1936 g for 7 min at room temperature. The cell pellets were resuspended in nuclei isolation buffer and again centrifuged at 1936 g for 7 min at room temperature. The cell pellets were then resuspended in nuclei isolation buffer containing 0.025% Empigen (nuclei isolation buffer+) and homogenized immediately with ten downward strokes using a tight Dounce-pestle. The cell lysates were centrifuged at 4336 g for 5 min. The nuclei pellets were washed in nuclei isolation buffer+. The nuclei were incubated on ice for 15 min in a series of buffers: HE (10 mM HEPES-NaOH, pH 7.5, 1 mM EDTA, and 0.1 mM PMSF), HE + 100 mM NaCl, HE + 500 mM NaCl, HE + 1 M NaCl, and HE + 2 M NaCl. After incubation with salt, centrifugation was performed to separate the nuclear solutions into supernatant and pellet fractions. The proteins in the supernatant fractions were precipitated using 17% TCA and cold acetone. Both pellets were suspended in sodium dodecyl sulfate-polyacrylamide gel electrophoresis (SDS-PAGE) buffer and subjected to 12.5% SDS-PAGE and subsequent Coomassie brilliant blue (CBB) staining and western blotting using anti-H2B (Millipore) and anti-mCherry (RFP) (MBL) antibodies.

EU and EdU labeling

EU and EdU incorporations were performed using Click-iT RNA imaging kits (Invitrogen) and Alexa Fluor 594 according to the manufacturer's instructions.

HaloTag labeling

H2B-HaloTags were stained with 1 nM HaloTag R110 Direct Ligand (Promega) for 1 hr and washed with 1 × HBSS.

Labeling of DNA replication domains

The scratch method was used to label DNA replication domains with Cy3-dCTP (Albiez et al., 2006). Briefly, in the presence of 200 nM or 20 μM Cy3-dCTP (GE), cells were scratched 200 times with a G27 fine needle. The background signals produced by free Cy3-dCTP were reduced by allowing the cells to enter 1 or 2 rounds of the cell cycle (24 h) after changing the medium. In addition, since the signal intensity of foci is 10- to 20-fold higher than single Cy3-dCTP and free (unincorporated) Cy3-dCTPs moved too quickly to be tracked in the time frame allotted, the signals produced by free ones are negligible. We thus tracked only foci movements, but not free ones.

Intracellular ATP measurement based on luciferase activity

HeLa S3 cells were grown in a 96-well culture plate (IWAKI) containing DMEM (Life Sciences) supplemented with 10% FBS. For ATP depletion, cells were incubated in a 96-well plate containing 10 mM sodium azide and 50 mM 2-deoxy-glucose in HBSS (GIBCO) for 30 min. Cells were then washed with HBSS. To measure ATP, the Cell ATP Assay Reagent (300–15363; Toyo B-Net CO., LTD.) was used according to the manufacturer's instructions. Bioluminescence was measured using a Lumat LB 9507 tube luminometer (EG & G BERTHOLD). Both the reaction and measurement were performed at room temperature in the dark. Incubation time from the addition of the assay reagent to measurement was exactly 10 min.

QUANTIFICATION AND STATISTICAL ANALYSIS

Data analysis for PALM imaging and single nucleosome tracking

Sequential microscopy images were converted to an 8-bit grayscale, and the background signals were subtracted using ImageJ software (NIH). The nuclear regions in the images were extracted. Following this step, the centroid of each fluorescent dot in each image

was determined, and its trajectory was tracked using u-track (MATLAB package) (Jaqaman et al., 2008). To generate PALM images based on the data, the nucleosome positions were mapped using R software (65 nm/pixel), and then a Gaussian blur (sigma = 1 pixel) was added to obtain smoother rendering using ImageJ.

For single-nucleosome movement analysis, the displacement and MSD of fluorescent signals were calculated based on the u-track data. The originally calculated MSD was in two dimensions. To obtain the three-dimensional value, the two-dimensional value was multiplied by 1.5 (4 to 6 Dt). Histograms of the displacement were prepared using KaleidaGraph (Synergy Software). To ascertain the position determination accuracy of the nucleosomes with H2B-PAmCherry, we calculated the standard deviation of two-dimensional movement of immobilized nucleosomes per 50 ms in FA-fixed cells (n = 10 molecules) and obtained 20.02 nm as the localization accuracy.

To generate a heatmap of domain dynamics, the median nucleosome movements (in 50 ms) in 3 × 3 pixels (65 nm/pixel) were calculated and plotted with a blue-to-red color scale using R.

Clustering analyses of nucleosomes in PALM images

The 2D RDF is given by the equation

$$g_{2D}(r) = \left[\left(\frac{S}{N-1}\right)\frac{1}{\pi(2r\Delta r + \Delta r^2)}\right]\left[\frac{1}{N}\sum_{i=1}^{N}\sum_{i\neq j}\delta(r - r_{i,j})\right],$$

where Δr = 10 nm is the binning width, and $(N-1)/S$ is the average particle density of S, which is the square of the total area. N is the total number of particles contained in the area. The factor $\pi(2r\Delta r + \Delta r^2)$ is the area of a ring of width Δr with a radius of $r + \Delta r$. The delta function is given by

$$\delta(r - r_{i,j}) = \begin{cases} 1, & (r - r_{i,j}) \leq \Delta r \\ 0, & others \end{cases},$$

where $r_{i,j}$ is the distance between r_i and r_j.

Ripley's K function is given by

$$K(r) = \left(\frac{S}{N-1}\right)\left[\frac{1}{N}\sum_{i=1}^{N}\sum_{i\neq j}\delta(r - r_{i,j})\right],$$

where $(N-1)/S$ is the average particle density of S, which is the square of the total area, and N is the total number of particles contained in the area. The delta function is given by

$$\delta(r - r_{i,j}) = \begin{cases} 1, & r_{i,j} \leq r \\ 0, & r_{i,j} > r \end{cases},$$

where $r_{i,j}$ is the distance between r_i and r_j.

The L function is given by

$$L(r) = \sqrt{\frac{K(r)}{\pi}}.$$

The area (S) of the total nuclear region was estimated using the Fiji plugin Weka, and the area of the whole region was measured by Analyze Particles.

Analysis of coherent movement of nucleosomes and replication foci

Dual-color labeling and imaging of the nucleosomes with H2B-Halo labeled with R110 and Cy3-incorporated DNA replication domains were performed using W-VIEW GEMINI (Hamamatsu Photonics). Cells expressing H2B-Halo were labeled with 1 nM R110 fluorescent dye. We selected closely localized H2B-Halo and DNA replication domains. Each movement of a spot was determined by ImageJ Fiji plug-in Particle Tracker. Similar movement trajectories in dual color were calculated over 10 continuous frames (500 ms) by the congruence coefficient (r_c) (Abdi, 2007) as described below:

$$r_c = \frac{\sum_{i,j} x_{i,j} y_{i,j}}{\sqrt{\left(\sum_{i,j} x_{i,j}^2\right)\left(\sum_{i,j} y_{i,j}^2\right)}}.$$

Let **X** and **Y** be I by J matrices of nucleosome and replication foci positions, respectively. X and Y are produced in the 10 continuous frames. I indicates the x-coordinate of the position and J the y-coordinate, so in this case we set I to 2 and J to 10. To align the center position of each trajectory in 10 frames, the average positions of X and Y were set to (0, 0) by subtracting the average position from

each position in each color respectively. Positions of H2B-Halo (R110) and Cy3dCTP were corrected by affine transformation. Parameters of affine transformation were estimated based on TetraSpeck bead imaging and calculated using the R package (vec2dtransf).

Analysis of nuclear volume

ESCs with and without LIF were treated with 0.5 μg/mL Hoechst 33342 for 30 min. HeLa cells were treated with/without 500 nM TSA for 2.5 hr and then additionally treated with 0.5 μg/mL Hoechst 33342 for 30 min. The z stacked images of labeled cell nuclei were observed using an Olympus FV-1000-D confocal laser scanning microscope (31 sections with a 500 nm thickness). The acquired z stack images were analyzed by the ImageJ plugin 3D Object Counter to measure the nuclear volume. n = 27 cells (with LIF), 29 cells (without LIF), 35 cells (with TSA), and 35 cells (without TSA).

Computer simulation of L-function plots for condensation and decondensation of chromatin domains

To examine changes in the L-function plots upon decondensation of chromatin domains, we performed computer simulations using a point distribution model. Here, we represented a nucleosome and a chromatin domain as a point and a cluster consisting of points, respectively. The random-distribution, circular-domain, and ellipse-domain (rod-like shaped) models were constructed using random numbers. In the circular domain model, first, we randomly generated center coordinates of N circles, with radius R, within a 100 × 100 square such that there was no overlap between the circles. Then M_{in} and M_{out} points were randomly generated inside and outside the circles, respectively. Parameters used in the circular-domain model (N, M_{in}/N, M_{out}/N and R) are listed and described in Figure S7. In the rod-like shaped model, points were generated similarly to the circle-domain model using randomly rotated ellipses with a semi-major axis of 20 and semi-minor axis of 5. Periodic boundary conditions were adopted to compute the L-functions for each model.

Computational modeling of a chromatin domain

We structurally modeled a chromatin domain using atomic coordinates of the nucleosome (PDB code: 1kx5). The modeling procedure was similar to that described in our previous paper (Maeshima et al., 2014). Here, the domain structure was modeled as follows. (i) The position and orientation of the first nucleosome were randomly generated within a sphere of 80-nm radius. (ii) The position and orientation of the second nucleosome were also randomly generated within the same sphere, so that the two nucleosomes were in contact. Two nucleosomes were considered to be in contact if the distance between the nucleosomes was greater than 6 nm and less than 18 nm, and if the minimum distance between two phosphor atoms of different nucleosomes was greater than 1 nm. (iii) The positions and orientations of the third and later nucleosomes were randomly generated within the sphere of 80-nm radius, so that the "incoming" nucleosome had at least two points of contact with prior nucleosomes. The numbers of nucleosomes in the domains (Figure 7C, left and right) are 646 and 1,000, and correspond to nucleosome concentrations of 0.50 and 0.78 mM, respectively.

DATA AND SOFTWARE AVAILABILITY

The raw data files for imaging data presented in this manuscript have been deposited to Mendeley Data and are available at http://dx.doi.org/10.17632/wr6zsbmshp.1.